Article

Human emissions drive recent trends in North Pacific climate variations

https://doi.org/10.1038/s41586-025-09368-2

Received: 31 January 2024

Accepted: 7 July 2025

Published online: 13 August 2025

Check for updates

Jeremy M. Klavans[1]✉, Pedro N. DiNezio[1], Amy C. Clement[2], Clara Deser[3], Timothy M. Shanahan[4] & Mark A. Cane[5]

The Pacific decadal oscillation (PDO)—the leading pattern of climate variability driving changes over the North Pacific and surrounding continents—is now thought to be generated by processes internal to the climate system[1,2]. According to this paradigm, the characteristic, irregular oscillations of the PDO arise from a collection of mechanisms involving ocean and atmosphere interactions in the North and tropical Pacific[3–5]. Recent variations in the coupled ocean–atmosphere system, such as the 2015 El Niño, ought to have shifted the PDO into its positive phase[6]. Yet, the PDO has been locked in a consistent downward trend for more than three decades, remanding nearby regions to a steady set of climate impacts. Here we show that the main multidecadal variations in the PDO index during the twentieth century, including the ongoing, decades-long negative trend, were largely driven by human emissions of aerosols and greenhouse gases rather than internal processes. This anthropogenic influence was previously undetected because the current generation of climate models systematically underestimate the amplitude of forced climate variability. A new attribution technique that statistically corrects for this error suggests that observed PDO impacts—including the ongoing multidecadal drought in the western United States—can be largely attributed to human activity through externally forced changes in the PDO. These results indicate that we need to rethink the attribution and projection of multidecadal changes in regional climate.

The Pacific decadal oscillation (PDO)—the leading mode of North Pacific sea-surface temperature (SST) variability[1,2]—is not oscillating. The ongoing, stubbornly persistent, cold phase of the PDO is associated with striking long-term trends in climate, including the rate of global warming[7] and drought in the western United States[8]. The leading conceptual models suggest that the PDO varies in response to an accumulation of processes internal to the climate system, including random atmospheric circulation variability, local ocean dynamics, and coupled tropical variability[3–5]. Statistical and dynamical models that simulate these processes predicted that the massive 2015 El Niño would finally reverse the sign of the obstinately persistent PDO[6]. Yet, the PDO and its associated impacts remain unchanged.

An alternative explanation for the PDO is that it reflects a North Pacific ocean–atmosphere response to external radiative forcings. However, the conventional understanding of the PDO does not include external radiative forcing. Recent review studies and the latest comprehensive report from the Intergovernmental Panel on Climate Change express 'high confidence' that multidecadal North Pacific climate variability is internally generated[3,5]. New research shows that large changes in the emissions of aerosols and greenhouse gases may explain recent multidecadal variations in North Atlantic and European climate[9–13], although this view is somewhat controversial[14]. A developing line of research hints that similar processes may be at play in the North Pacific[15–21], but this work cannot fully explain the persistence of the ongoing negative phase of the PDO or why models underestimate levels of PDO variance[5,22,23].

Here we isolate anthropogenic influences on multidecadal North Pacific climate variability using an exceptionally large ensemble of climate model simulations. We characterize climate variability in the North Pacific using the first principal component of North Pacific annual average SST anomalies as a PDO index[2]. We calculate these anomalies by removing the annual cycle and subtracting the global mean temperature[2]. This definition, which avoids the constraint that the PDO must be orthogonal to global temperature rise[2], is widely used in recent mechanistic and impact studies of the PDO[3,8], and we wish to bring PDO impacts to the forefront. We calculate the PDO index in each of the 572 simulations in the multimodel ensemble, all of which are forced by a combination of all the main sources of external forcing, including greenhouse gas and aerosol emissions, volcanic eruptions and solar variability (Extended Data Table 1). Averaging the historical PDO indices simulated by all ensemble members cancels out uncorrelated, naturally generated variations in climate, showing the externally forced influence common to all simulations. We further isolate individual sources of external forcing by considering three single-forcing large ensembles, each of which includes changes in only one forcing agent at a time (Extended Data Table 1). The bulk of our analysis focuses

[1]Department of Atmospheric and Oceanic Sciences, University of Colorado Boulder, Boulder, CO, USA. [2]Rosenstiel School of Marine, Atmospheric, and Earth Science, University of Miami, Miami, FL, USA. [3]National Center for Atmospheric Research, Boulder, CO, USA. [4]Jackson School of Geosciences, University of Texas at Austin, Austin, TX, USA. [5]Lamont Doherty Earth Observatory, Columbia University, New York, NY, USA. ✉e-mail: jeremy.klavans@colorado.edu

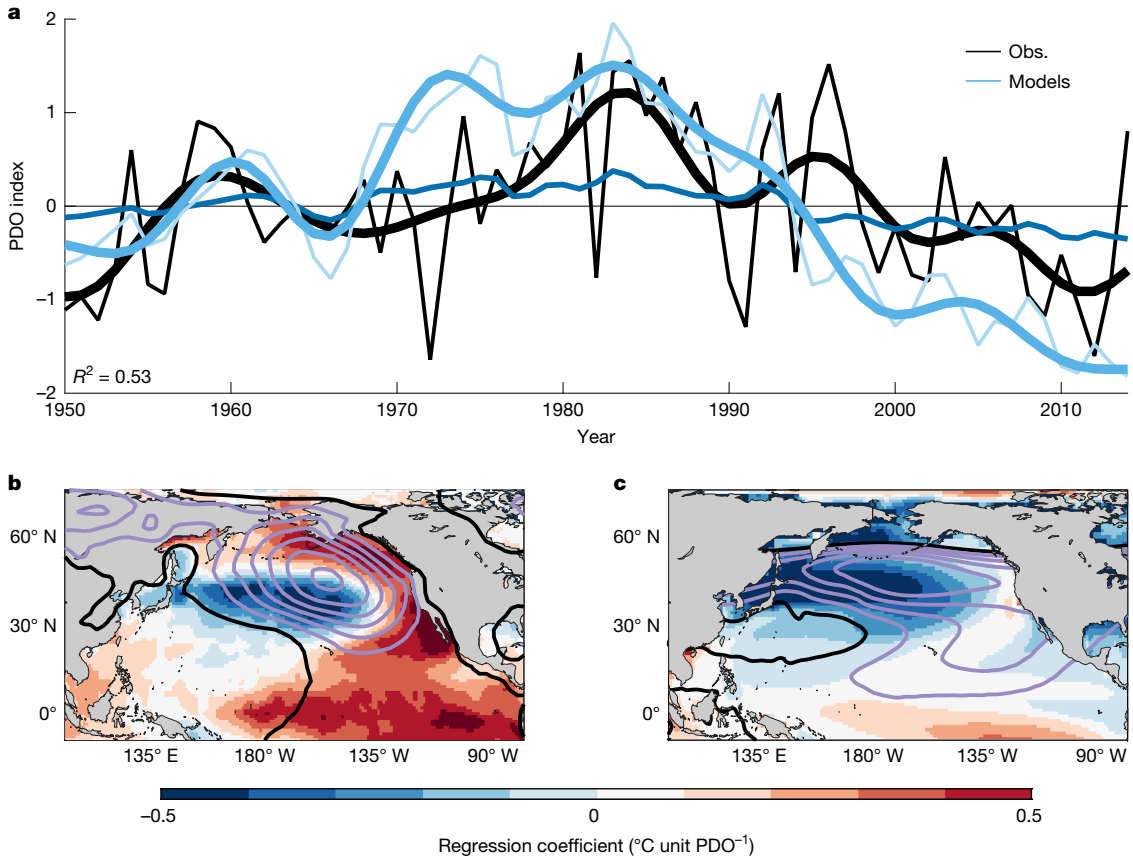

Fig. 1 | External forcing explains the timing and pattern of the PDO. **a**, The observed PDO index from HadISST[51] with ENSO linearly removed (black) compared with the ensemble mean PDO index from the all-forcings simulations[52–62] (dark blue) and the normalized ensemble mean PDO index from the all-forcings simulations (light blue). We normalize the forced PDO index by setting the standard deviation (σ) to 1 to maintain consistency with the traditional definition of the PDO index[1] and to illustrate the timing of the shifts in both indices; the amplitudes of each timeseries are listed in Extended Data Table 2b and discussed in the text. The R^2 value at the bottom left is the square of the correlation between the observed (ENSO removed) and ensemble mean PDO indices. **b**, Regression of observed SST from HadISST[51] (colours; °C per unit of the PDO index) and sea-level pressure from NCEP twentieth-century reanalysis[63] (contours; hPa per unit of the PDO index) on the observed PDO index. The KOE region is outlined in the solid black rectangle. **c**, Regression of ensemble mean SST (colours) and sea-level pressure (contours) on the normalized, ensemble mean PDO index from the all-forcing simulations (see text for details). In **b** and **c**, SLP regressions are contoured every 0.5 hPa; negative values are in purple and the zero contour is in black (there are no positive values).

on the 1950–2014 period common to all simulations, although we consider the full length of simulations dating back to 1850 when possible. On interannual timescales, the PDO index is, in part, driven by the El Niño–Southern Oscillation (ENSO), a prominent source of naturally generated variability[3,24]. As noted above, ensemble averaging removes the influence of the internal component of ENSO on the PDO index in models[2,25,26]. We linearly remove variability associated with the Niño 3.4 index from the observed PDO index to isolate the sources of multidecadal variability that are the focus of this study (Methods). Although this approach slightly alters the interannual timing of the observed PDO index, it has limited effect on the multidecadal shifts in the index that we are seeking to explain (Extended Data Fig. 1). Finally, we use a low-pass filter on both the observed and simulated PDO indices to isolate variability with periods longer than 10 years (Methods).

A new, forced component of the PDO

We find that changes in external forcing explain key recent multidecadal shifts in observed North Pacific climate. Between 1950 and 2014, we estimate that the externally forced PDO index explains 53% of observed multidecadal PDO index variance (R^2) and reproduces major PDO transitions in the 1970s and 1990s to within a few years, even without accounting for tropical Pacific variability (Fig. 1a). External forcing explains 46% of PDO index variance in a stricter, alternative definition of the PDO index, in which North Pacific regional temperatures are subtracted (rather than global mean temperatures) to ensure that our conclusions are not an artefact of a known relationship between Pacific climate variability and global mean temperatures[27] (Extended Data Fig. 2a). Likewise, external forcing explains 48% of the detrended, decadal SST variance in the crucial Kuroshio–Oyashio Extension (KOE) region, demonstrating that our results are not an artefact of the traditional approach to isolating PDO variability with empirical orthogonal functions (Extended Data Fig. 3a). The reported levels of variance explained for the traditional PDO index, the PDO index with North Pacific SSTs removed and the KOE SST index are statistically significantly different from zero at the 4%, 6% and 4% levels, respectively, using a non-parametric statistical test that accounts for serial correlation in low-pass filtered timeseries (Methods and Extended Data Fig. 2d).

The above statistical tests do not account for the possibility that internal variability in observations happens to align with the ensemble mean, thereby amplifying the reported correlation coefficients by chance. We find this possibility to be unlikely. The model-estimated, forced PDO index explains more variance in the observed PDO index than more than 99% of the model-generated realizations of internal variability (568 out of 572; Fig. 2a). That is, in models, there is less than a 1% chance (4 out 572 realizations) that internal variability alone explains

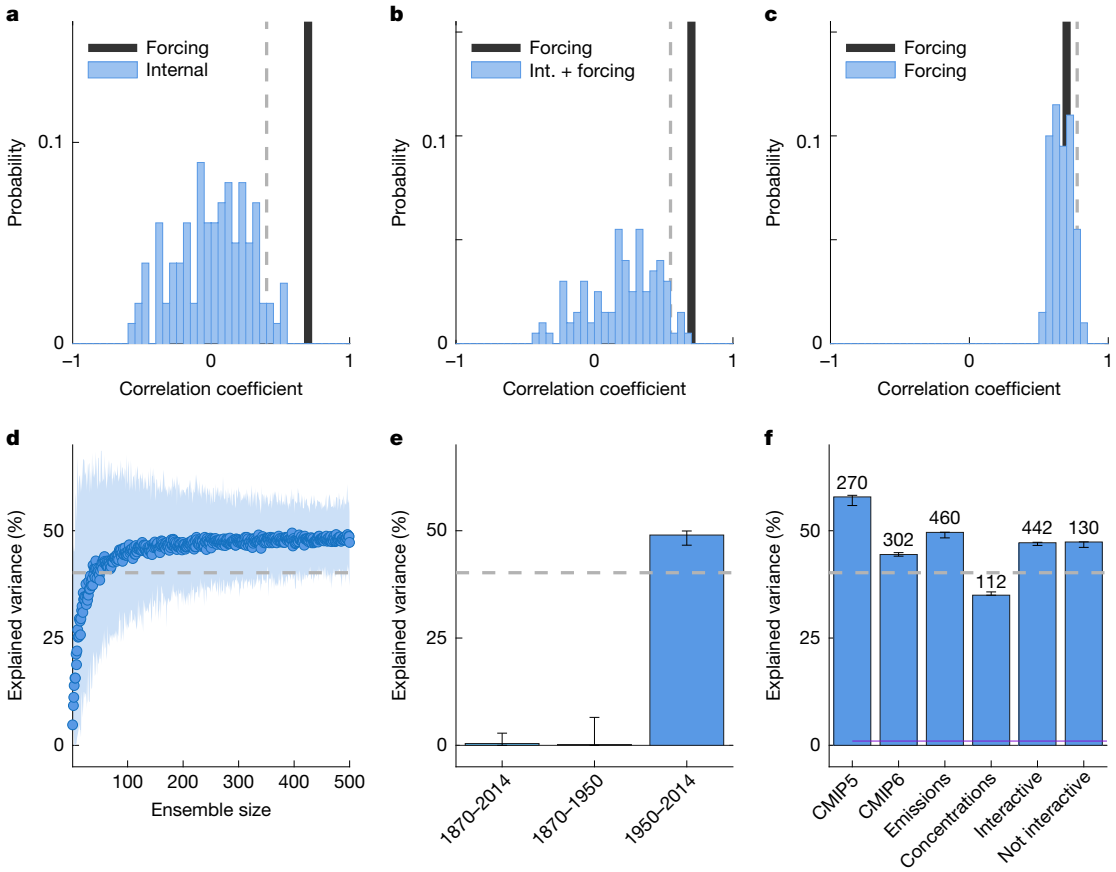

Fig. 2 | The role of forcing in the PDO is statistically robust. a, Comparison of the correlation coefficient between the internally generated PDO indices in individual ensemble members[52–62] and observations from HadISST[51] (blue histogram) with the correlation coefficient of the ensemble mean and observation (black line). The empirical 90% confidence level (two-tailed) for the distribution of correlations is shown as a light grey line. **b**, As in **a**, but for the PDO index from each individual ensemble member, which includes internally generated and externally forced variability. **c**, As in **a** and **b**, but for bootstrapped 100-member ensemble means that show different estimates of the externally forced response. **d**, The level of PDO variance explained by external forcing, as a function of ensemble size. For each ensemble size, we randomly select members from the full ensemble, average and correlate with observations to calculate the mean explained variance (dot) and the 95% confidence interval (cloud). We also test the null hypothesis that the correlation is zero at the 90% confidence level by an empirical significance test that accounts for autocorrelation (grey dashed line; Methods). We can produce a conservative estimate of the ensemble size required to isolate the forced PDO by intersecting the bottom of the confidence interval at 500 members with the mean variance explained. **e**, The contribution of external forcing to the PDO as a function of time. Error bars are calculated by bootstrapping new ensemble means (with replacement) to test our isolation of the forced response (Methods). We test the null hypothesis that the correlation illustrated by the third bar (1950–2014) is zero using an empirical test that accounts for autocorrelation. The 90% confidence interval is plotted in the grey dashed line. **f**, Level of explained variance in the ensemble subdivided by key traits (Extended Data Table 1). Again, the 90% confidence interval is plotted in the grey dashed line.

the correlation between the ensemble mean and observations (Fig. 2a). Likewise, the model-estimated, forced PDO index explains more variance in the observed PDO index than in 98% of the individual model simulations (560 out of 572; Fig. 2b). That is, in models, there is a 2% chance (12 out of 572 realizations) that internal variability aligns with external forcing to increase the apparent share of forced variance in the PDO (Fig. 2b). Conversely, external forcing can consistently explain the large correlation we report above (Fig. 2c).

Signal-to-noise error in the North Pacific

Our approach was able to isolate this unexpectedly large influence of external forcing on the PDO because of the extremely large number of model simulations that have recently become available. We estimate that more than 70 individual ensemble members are required to isolate the forced component of the PDO; that is, 70 members are needed to reach a correlation with observations that is not significantly different (at the 95% level) from the estimate from the full ensemble (Fig. 2d and Extended Data Fig. 4). These extraordinarily large datasets are needed because models underestimate the amplitude of the forced component of the PDO. In observations, external forcing accounts for 53% of total multidecadal PDO amplitude, whereas in models, external forcing only accounts for 7% of total multidecadal PDO amplitude (Methods). This error is also apparent in the KOE SST index, for which external forcing accounts for 48% of observed multidecadal variance and 7% of simulated multidecadal variance. Put succinctly, in models, the ratio of the externally forced signal to internally generated noise in the multidecadal PDO is much lower than in observations. Consequently, the much too large internally generated noise overwhelms the forced PDO and KOE SST signals in the individual simulations of historical climate. This signal-to-noise error is also apparent in simulations of North Atlantic climate variability, indicating that this error may affect low-frequency modes of climate variability throughout the extratropical Northern Hemisphere, and potentially globally[11,28,29].

Human-forced trends in the PDO index

The contribution of external forcing to the PDO grows as external forcing intensifies throughout the twentieth century. Before the mid-twentieth century, PDO variability in models seems to be largely

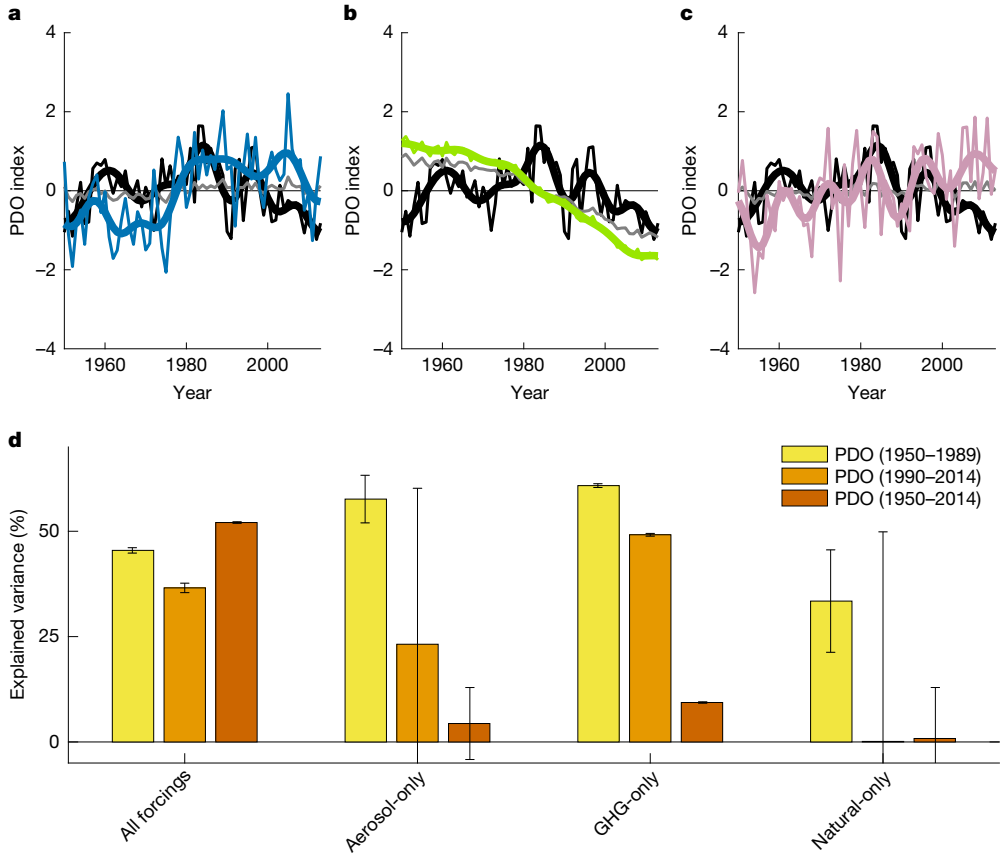

Fig. 3 | Forcing from anthropogenic aerosols and greenhouse gases explain the timing of recent trends in the PDO index. a–**c**, The forced PDO index from the aerosol-only simulations (**a**), greenhouse gas-only simulations (**b**) and the natural forcing-only simulations[64] (**c**) compared with the PDO index from annual average (thin black line) and low-pass filtered observations (thick black line; HadISST[51]). The original amplitude PDO index from each single-forcing ensemble is shown as the thin grey line. **d**, The amount of observed PDO variance explained by the ensemble mean of each of the four suites of simulations for 1950–1989, 1990–2014 and 1950–2014 (bars) and their 90% confidence interval calculated by bootstrap as in Fig. 2d. This statistical test accounts for uncertainty in the forced response. A statistical test that compares these correlations with that which would have been produced from internal variability is presented in Extended Data Table 3. Note that the correlation between the forced PDO in the GHG-only ensemble and observations between 1950 and 1989 is negative.

internally generated by the climate system (Fig. 2e). Between 1870 and 1950, external forcing explains less than 1% of multidecadal PDO variance (Fig. 2e). However, after the mid-twentieth century, as changes in forcing increase, so too does the role of external forcing in the PDO (Fig. 2b and Extended Data Fig. 5). Likewise, the variance of the forced component increases after the mid-twentieth century for both the PDO index and the KOE SST index (Extended Data Table 2a). The variance of internal KOE temperature variability in models does not change between 1870 and 2014, as in the North Atlantic[30], suggesting that signal and noise may be additive in climate models (Extended Data Table 2b). Previous studies may have underestimated this newfound role of forcing in the PDO for two reasons: (1) they could only use small ensembles; and (2) they may have convolved the relatively unforced first half of the twentieth century with the intensifying forcing of the second half of the twentieth century. For example, in an average 40-member ensemble run from 1920 to 2005 (as in ref. 3), external forcing explains only 5% of multidecadal PDO variance. To detect the role of forcing in the modern PDO, we must use an exceptionally large ensemble and focus on the late twentieth century (that is, after 1950), when changes in forcing were larger.

The size and breadth of this ensemble allow us to demonstrate the robustness of this new, larger role for external forcing in the PDO. First, we find that both single-model ensembles (CESM2 and MPI) that meet the criterion of 70 members to sufficiently isolate the forced PDO (Fig. 2d) have a statistically significant forced component (Extended Data Fig. 5). Although it is likely that there are inter-model differences in the amplitude of the forced response, the signal-to-noise error makes it difficult to make definitive statements about single-model ensembles with less than 70 members. Instead, we group models by their common attributes and create large enough ensembles to isolate the impact of these features on the forced PDO. We find that the contribution of forcing to the PDO is reasonably robust to (1) model generation, that is, CMIP5 or CMIP6; (2) the implementation of aerosol emissions; and (3) the complexity of cloud–aerosol interactions (Fig. 2f and Extended Data Table 3). That is, both the anthropogenic influence on the PDO and the signal-to-noise error in the forced response are robust across models despite their diverse representations of physical processes (Extended Data Table 3). Together, these sensitivity analyses show that the substantial role for external forcing in the timing of the PDO index is not an artefact of a single model, numerical approach or physical process, such as the implementation of aerosol indirect effects.

Models show that the observed timing of multidecadal shifts in the PDO index is influenced by a combination of anthropogenic aerosols and greenhouse gases. Between 1950 and the mid-1980s, rapidly rising concentrations of industrial aerosols[31] coincide with a positive trend in the PDO index (Fig. 1a and Extended Data Table 3). When forced with only industrial aerosols, models also simulate a positive PDO trend over that period (Fig. 3a,d and Extended Data Table 3). In the late 1980s, the observed positive PDO trend reverses in association with stagnating aerosol emissions and the predominance of greenhouse gas warming[5] (Figs. 1a and 3a,b and Extended Data Table 3). The observed negative trend in the PDO after the mid-1980s is captured in the all-forcing runs and is even stronger when models are forced with only greenhouse

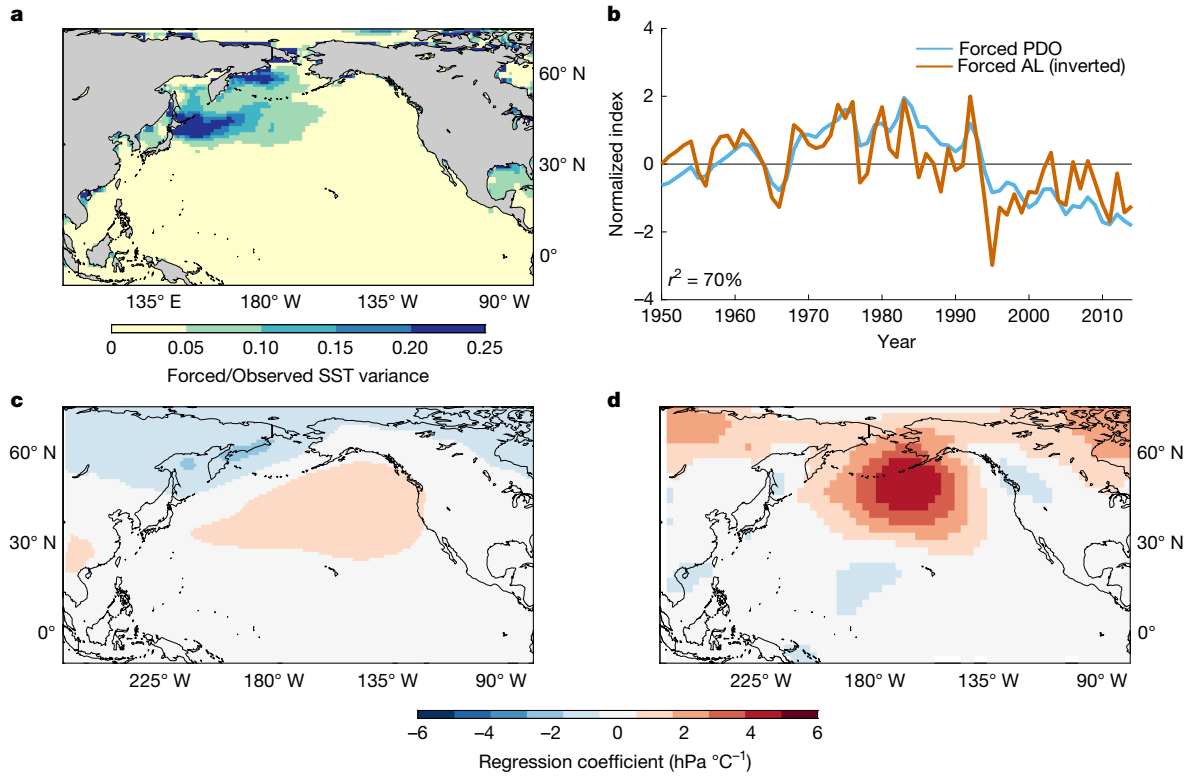

Fig. 4 | The signal-to-noise paradox in the PDO is associated with weak Aleutian Low variability. a, The ratio of forced SST variance from models[52–62] to total observed SST variance in models. **b**, Time series of the forced PDO (from Fig. 1a) along with the strength of the forced Aleutian Low (as described by the North Pacific Index; Methods). **c**, The regression of forced sea-level pressure on an index of forced SST in the KOE region (Fig. 1b), which indicates the strength of the association between the forced atmospheric response and the forced SST changes. **d**, The regression of observed sea-level pressure on the index of observed SST in the KOE region, which indicates the strength of the association between the observed atmospheric response and the observed SST changes (HadISST[63]).

gases, which drive a negative trend in the PDO (Fig. 3b,d and Extended Data Table 3). We note that the short length of this subsection of the record limits its statistical significance (Extended Data Table 3). However, these trends have continued and intensified to the present day, consistent with our argument. We suggest that stagnating industrial aerosol concentrations paired with rising greenhouse gas concentrations halted the rise in the PDO index in the mid-1980s and produced the negative trend in the PDO index that continues into the present. Both anthropogenic aerosols and greenhouse gases can force changes in the PDO, whereas small changes in natural forcings—that is, from solar cycles and volcanic eruptions—explain only a small part of the temporal evolution of the PDO over our study period (R^2 = 1%; Fig. 3c,d).

Potential mechanisms for the forced PDO

In addition to explaining key observed shifts in the PDO, the forced PDO index is associated with an SST pattern in models that bears key resemblances to both the observed PDO pattern and the internally generated PDO pattern in models. In the PDO positive phase, the observed and simulated SST patterns both show cooler-than-normal ocean temperatures over the western and central North Pacific, surrounded by a horseshoe of relatively warmer surface waters along the North American coast (Fig. 1b,c and Extended Data Fig. 6). Similar to the real world, the positive phase of the forced PDO in models is associated with a deepening of pressure near the Aleutian Low, the semi-permanent low-pressure system controlling surface winds over the North Pacific (Fig. 1c, contours). If the PDO index were purely internally generated, this pattern would not appear in the regression on the ensemble mean because it would cancel out across many ensemble members. The general features of the forced PDO pattern are robust across model generations, individual model ensembles and how models represent complex physical processes (Extended Data Figs. 6–8). Yet, the multi-model mean and most individual ensembles exhibit a key deficiency: the horseshoe-shaped pattern of warming along the coast of North America in the positive phase of the PDO seems to be weaker in models than observations (Fig. 1b,c and Extended Data Figs. 6–8). This deficiency seems to be related to the ability of the models to generate the full PDO pattern, not just its externally forced component (Extended Data Fig. 6).

The discrepancy between the spatial patterns in observations and the ensemble mean may provide a clue as to why the forced PDO is too weak in models. The horseshoe-shaped pattern of temperature anomalies is characteristic of the well-established simultaneous relationship between the Aleutian Low and North Pacific SSTs in observations[3]. In models, we find that the forced, multidecadal PDO index is highly correlated with forced variations in the strength of the forced, multidecadal Aleutian Low (R^2 = 0.7; Fig. 4b and Methods). This indicates that either variations in the Aleutian Low drive changes in the PDO SST pattern[3] or SST variations, particularly in the KOE region, can drive changes in the overlying Aleutian Low[32–34]. Either of these potential responses could be excited by hemispheric warming or cooling, including contemporaneous forced North Atlantic climate variability[35] or over nearby continents[36,37].

Any of these pathways would rely on an amplifying feedback over the KOE region, in which oceanic thermal advection by wind-driven ocean currents reinforces SST variability[38]. We find that the strength of the relationship between the Aleutian Low and SSTs is much weaker in models (average ensemble member 1.5 hPa °C^{-1} and forced component 0.9 hPa °C^{-1}; Fig. 4c) than in observations (5 hPa °C^{-1}; Fig. 4d), which we quantify by regressing sea-level pressure variations on SST variations in the KOE region. This suggests that in models, perturbations fail to excite

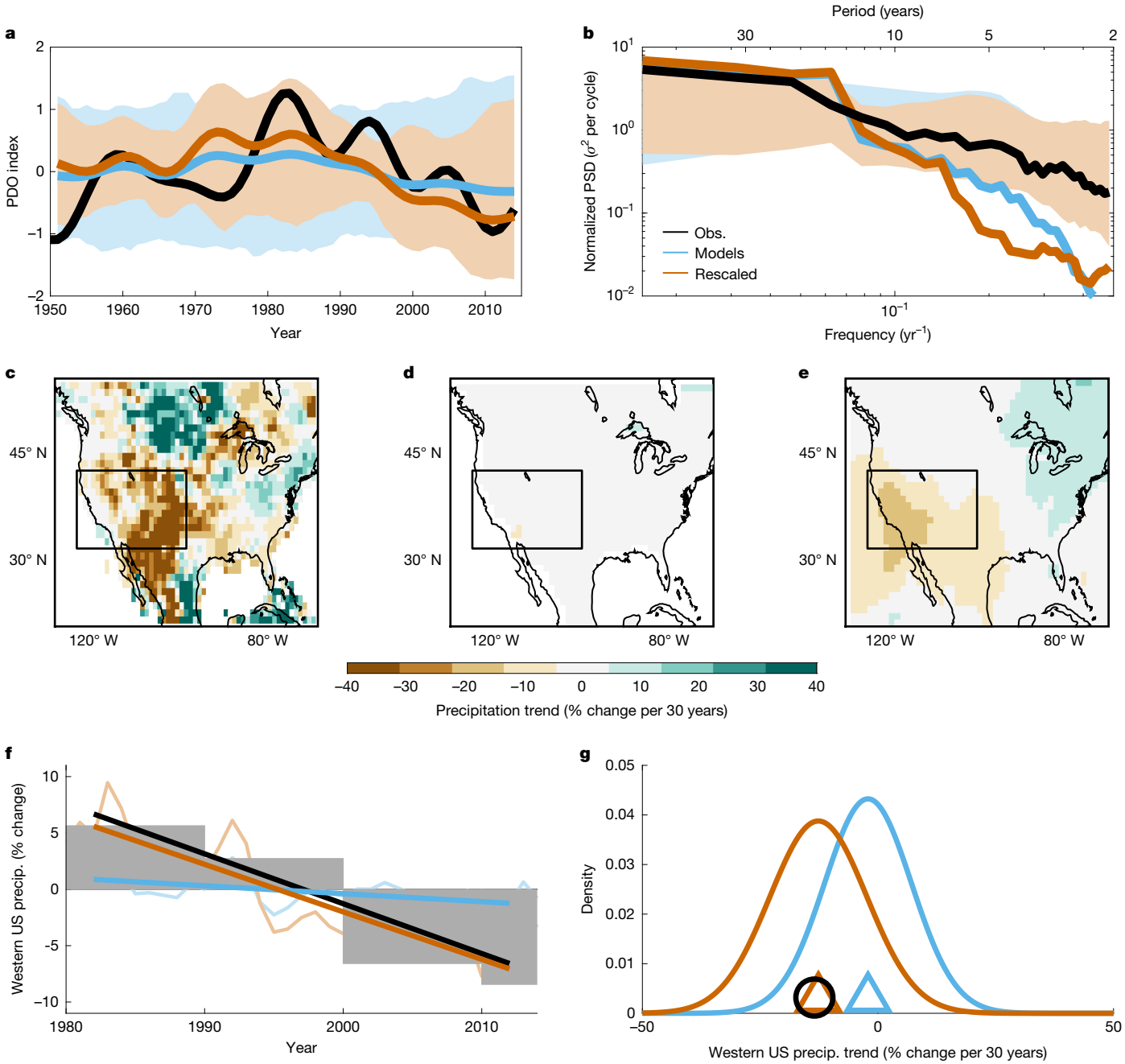

Fig. 5 | The long-term meteorological drought in the western United States is attributable to human emissions of aerosols and greenhouse gases by their influence on the PDO. a, The PDO indices from observations from HadISST[63] (black), the all-forcings large ensemble[52–62] (ensemble mean in the blue line and the 2σ ensemble spread in the blue shading), and the corrected ensemble (ensemble mean in the orange line and the 2σ ensemble spread in the orange shading). **b**, Spectra of the PDO indices from observations (black), the all-forcings ensemble (ensemble mean in the blue line and the 2σ ensemble spread in the blue shading) and the corrected ensemble (ensemble mean in the orange line and the 2σ ensemble spread in the orange shading). **c**–**e**, Maps of water year (October to September) precipitation trends between 1983 and 2012 in observations from GPCP[65], in which the ENSO-related pattern of precipitation has been removed (**c**), the all-forcings ensemble (**d**) and the corrected ensemble (**e**). **f**, Decadal mean precipitation changes in the western United States (31°–42° N, 125°–100° W) from observations, in which ENSO has been removed (grey bars) and the timeseries of the forced precipitation changes from the all-forcings large ensemble (light blue) and the corrected ensemble (light orange). The best-fit linear trend is plotted for observations (black), the all-forcings ensemble mean (blue) and the corrected ensemble mean (orange). **g**, Precipitation trends in the western United States from observations (black circle), the all-forcings ensemble mean (blue triangle), the corrected ensemble mean (orange triangle) and probability density functions of the trends from individual all-forcing ensemble simulations (blue curve) and the corrected ensemble (orange curve).

a response in the Aleutian Low with the same vigour as that in the real world. This mismatch might occur because of either poor simulation of the direct influence of forcing on the atmosphere or an underestimated positive feedback involving KOE SSTs[39]. In either case, these underestimated mechanisms could help explain the underestimated amplitude and persistence of the forced PDO in models.

Impacts of the forced PDO negative trend

The failure of climate models to simulate the full amplitude of the forced PDO has clouded our view of the recent history of global and regional climate. In the early 2000s, a hiatus in global warming was largely attributed to a naturally generated PDO-like pattern of cooling

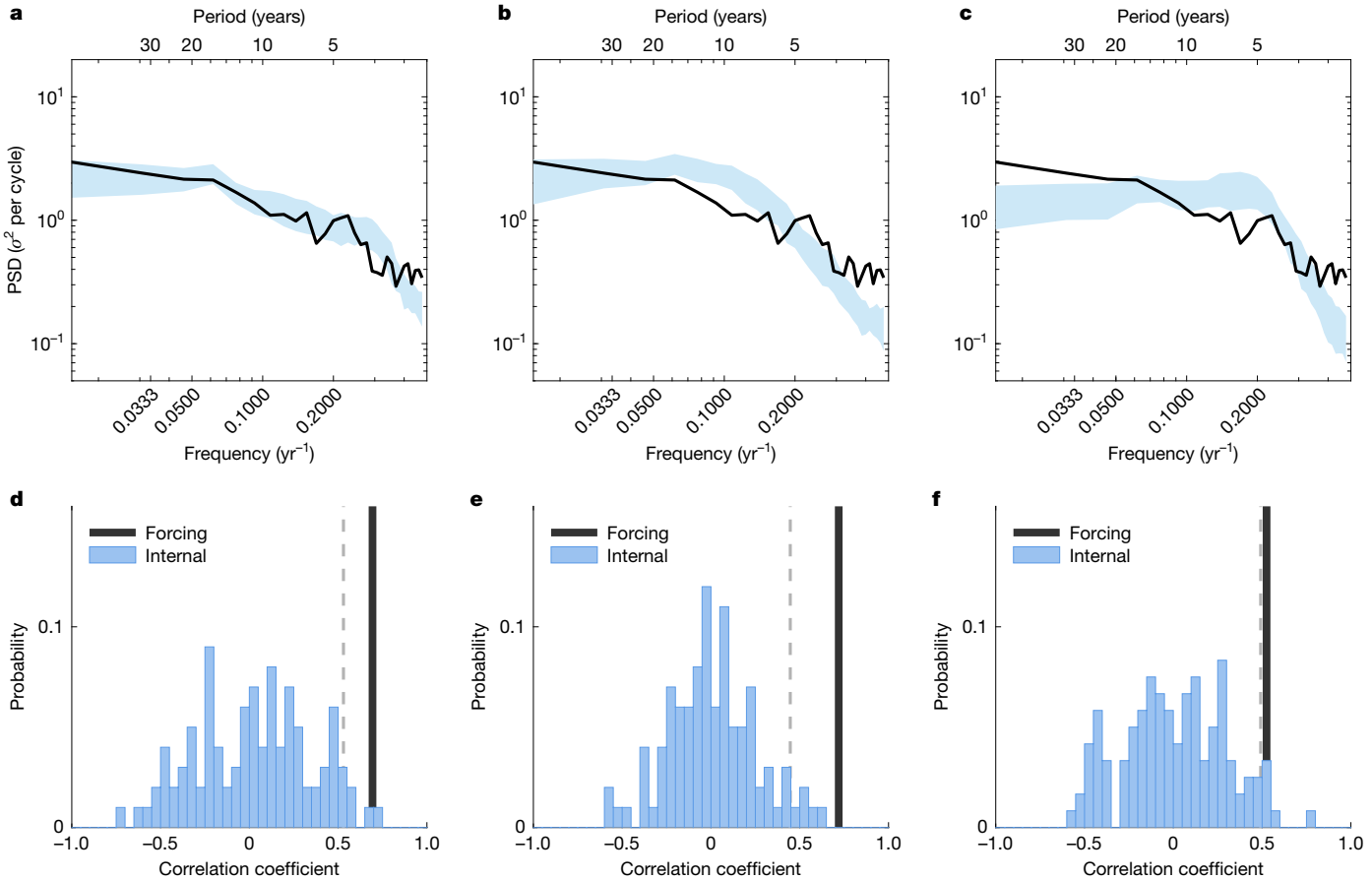

Fig. 6 | A stronger internal PDO in models does not solve the signal-to-noise error. Here we compare the two single-model ensembles with the largest (most realistic) PDO variance (**a**,**b**,**d**,**e**) with the multimodel ensemble composed of the three single-model ensembles with the lowest (least realistic) PDO variances[52–62]. **a**–**c**, The normalized power spectra of the observed PDO from HadISST[51] (black) and interquartile range of PDO indices produced by individual ensemble members (blue cloud). **d**–**f**, Comparison of the correlation coefficient between the internally generated PDO indices in individual ensemble members and observations (blue histogram) with the correlation coefficient of the ensemble mean and observation (black vertical line). The empirical 90% confidence level (two-tailed) for the distribution of correlations is shown as a light grey vertical line.

in the Pacific Ocean[7]. However, we have shown that forcing excites this pattern on multidecadal timescales, but its influence is underestimated by climate models. Mitigating the signal-to-noise error in climate models will amplify the forced PDO so that they will better account for global mean temperatures at the beginning of the twenty-first century. Furthermore, by mitigating this error in models, we may also rectify known biases in the simulation of externally forced trend in the tropical Pacific[40]. Although here we demonstrate that forcing excites the PDO pattern in isolation from the tropics, climate variability in these two regions is intertwined[3]. Overall, climate models incorrectly simulate a forced El Niño-like trend in the tropical Pacific over the past few decades[41], which is at odds with the neutral or La Niña-like trend in observations and theory[40,42]. This erroneous trend seems to be uniquely within the tropics[25]. We show that the ongoing negative trend in the extratropical PDO, including the associated cooling that extends into the eastern tropical Pacific, is underestimated by models. If the signal-to-noise error were to be corrected in models, it follows that the cooling simulated by models in the eastern tropical Pacific could be enhanced through the extratropical influence of the forced PDO to be brought into better agreement with observations.

The meteorological drought in the western United States is currently thought to be internally generated by a natural, albeit unlucky, combination of variations in the climate system. This idea prevails because climate models do not explain the magnitude of the observed precipitation decline[43]. However, it is established that the PDO is associated with precipitation in the western United States[44]. Thus, our findings that models underestimate the forced response of the PDO suggest that the meteorological drought has a large anthropogenic component. We correct for this error by setting the signal-to-noise ratio in models equal to our estimate of that in observations[29] (Methods). We retain random interannual variability in each ensemble member but reduce its amplitude and increase the amplitude of the forced PDO and associated impacts (Fig. 5a,b). After this correction for the signal-to-noise error, we find a much larger precipitation deficit in the western United States than the original ensemble (−12.6% compared with −2.1% of climatology per 30 years), bringing them close to observations (−13.3%; Fig. 5c–e). Negative precipitation trends as large as observed are commonplace in the statistically corrected ensemble but were rare in the original ensemble (47% of simulations compared with 12%). Correcting for the signal-to-noise error in climate models attributes nearly all of the observed long-term precipitation decline over the past few decades to anthropogenic forcing, through the forced PDO. In addition to the forced PDO, there is also a role for internally generated tropical Pacific SST variability in setting the precipitation rates over the western United States[43,45]. A complete analysis of the role of forcing in the meteorological drought would have to account for uncertainty in the magnitude of the signal-to-noise error in PDO impacts, how the signal-to-noise error changes in response to different combinations of forcing agents and the possibility that observed internal variability confounds our estimate of the observed, forced signal. We find the last of these sources of uncertainty unlikely to influence our results (Methods).

Although our results emphasize the newfound role for external forcing in the PDO and its impacts, internal variability is an important contributor, especially on interannual and shorter timescales. For example, internal variations in ENSO influence the PDO on interannual timescales[3,6] and, therefore, accurate ENSO predictions can add skill to near-term PDO predictions. Model errors in the tropical Pacific or elsewhere may deleteriously influence our results on the PDO and its impacts, as in any study reliant on models. Because our estimate of the magnitude of the forced PDO is based on correlations, underestimating the internal component of the PDO[22] is an error that does not affect our results (Methods). A subset of models with a realistic internally generated PDO produce a forced PDO that is well-correlated with observations but still exhibit the signal-to-noise error, as in the full ensemble (Fig. 6). Thus, our estimates of the role of external forcing in the PDO stand up to knowable forms of uncertainty but are still bound by the limitations of any modelling study.

Forced PDO portends future drought

Overall, we find that human activity is a key contributor to multi-decadal trends in the PDO since the 1950s. Aerosol emissions influenced the positive trend in the PDO from the 1950s to 1980s. The abatement of industrial aerosol emissions paired with exponentially rising greenhouse gas emissions are influencing the ongoing negative trend in the PDO. This history of external forcing can thus explain a statistically significant portion of multidecadal PDO impacts over the past seven decades, including the ongoing drought in the western United States, as shown here. The role of external forcings in the PDO was obscured by an unrealistically low signal-to-noise ratio in climate models, which we can expose only because we now have an extraordinarily large ensemble of climate model simulations. We suggest that the small amplitude of the forced PDO is related to an underestimated Aleutian Low response to external forcing in models. By identifying this error in the North Pacific, we have added to the results for the North Atlantic[11], showing that the signal-to-noise error is a pervasive problem across the extratropics in the Northern Hemisphere. Resolving the signal-to-noise error, therefore, offers the prospect of improvements in predictive skill for regional climate in climate models based on the projections of external forcing. At the very least, it would allow equivalent skill with far smaller ensembles.

Model improvements, such as increasing spatial resolution, may help mitigate the signal-to-noise error[46,47] by improving the simulation of both oceanic[48,49] and atmosphere–ocean feedbacks[39,50]. Of course, model development is expensive and time-consuming. Although we await improvements in models, reinterpretation of the existing catalogue of climate model output holds the potential to improve our understanding and ability to project regional climate changes. For example, because of the signal-to-noise error in climate models, the prevailing view has been that the ongoing historical western United States meteorological drought is a natural variation associated with the oscillating internal PDO. Thus, it is expected to abate when the PDO reverses sign. In our reinterpretation of model output, we project that so long as ongoing anthropogenic forcing trends continue, the PDO will remain persistent in its negative state, driving continued precipitation deficits in the western United States. The difference is highly consequential.

Online content

Any methods, additional references, Nature Portfolio reporting summaries, source data, extended data, supplementary information, acknowledgements, peer review information; details of author contributions and competing interests; and statements of data and code availability are available at https://doi.org/10.1038/s41586-025-09368-2.

1. Mantua, N. J., Hare, S. R., Zhang, Y., Wallace, J. M. & Francis, R. C. A Pacific interdecadal climate oscillation with impacts on salmon production. *Bull. Am. Meteorol. Soc.* **78**, 1069–1080 (1997).
2. Zhang, Y., Wallace, J. M. & Battisti, D. S. ENSO-like interdecadal variability: 1900–93. *J. Clim.* **10**, 1004–1020 (1997).
3. Newman, M. et al. The Pacific decadal oscillation, revisited. *J. Clim.* **29**, 4399–4427 (2016).
4. Latif, M. & Barnett, T. P. Causes of decadal climate variability over the North Pacific and North America. *Science* **266**, 634–637 (1994).
5. Eyring, V. et al. in *Climate Change 2021: The Physical Science Basis*. Contribution of Working Group I to the Sixth Assessment Report of the Intergovernmental Panel on Climate Change (eds. Masson-Delmotte, V. et al.) 423–552 (Cambridge Univ. Press, 2021).
6. Meehl, G. A., Hu, A. & Teng, H. Initialized decadal prediction for transition to positive phase of the Interdecadal Pacific Oscillation. *Nat. Commun.* **7**, 11718 (2016).
7. Trenberth, K. E. & Fasullo, J. T. An apparent hiatus in global warming? *Earths Future* **1**, 19–32 (2013).
8. McCabe, G. J., Palecki, M. A. & Betancourt, J. L. Pacific and Atlantic Ocean influences on multidecadal drought frequency in the United States. *Proc. Natl Acad. Sci. USA* **101**, 4136–4141 (2004).
9. Borchert, L. F. et al. Skillful decadal prediction of unforced southern European summer temperature variations. *Environ. Res. Lett.* **16**, 104017 (2021).
10. Booth, B. B. B., Dunstone, N. J., Halloran, P. R., Andrews, T. & Bellouin, N. Aerosols implicated as a prime driver of twentieth-century North Atlantic climate variability. *Nature* **484**, 228–232 (2012).
11. Klavans, J. M., Cane, M. A., Clement, A. C. & Murphy, L. N. NAO predictability from external forcing in the late 20th century. *npj Clim. Atmos. Sci.* **4**, 22 (2021).
12. Menary, M. B. et al. Aerosol-forced AMOC changes in CMIP6 historical simulations. *Geophys. Res. Lett.* **47**, e2020GL088166 (2020).
13. He, C. et al. Tropical Atlantic multidecadal variability is dominated by external forcing. *Nature* **622**, 521–527 (2023).
14. Zhang, R. et al. A review of the role of the Atlantic meridional overturning circulation in Atlantic multidecadal variability and associated climate impacts. *Rev. Geophys.* **57**, 316–375 (2019).
15. Wang, T., Otterå, O. H., Gao, Y. & Wang, H. The response of the North Pacific decadal variability to strong tropical volcanic eruptions. *Clim. Dyn.* **39**, 2917–2936 (2012).
16. Yeh, S.-W. et al. Changes in the variability of the North Pacific sea surface temperature caused by direct sulfate aerosol forcing in China in a coupled general circulation model. *J. Geophys. Res. Atmos.* **118**, 1261–1270 (2013).
17. Boo, K.-O. et al. Influence of aerosols in multidecadal SST variability simulations over the North Pacific. *J. Geophys. Res. Atmos.* **120**, 517–531 (2015).
18. Diao, C., Xu, Y. & Xie, S.-P. Anthropogenic aerosol effects on tropospheric circulation and sea surface temperature (1980-2020): separating the role of zonally asymmetric forcings. *Atmos. Chem. Phys.* **21**, 18499–18518 (2021).
19. Smith, D. M. et al. Role of volcanic and anthropogenic aerosols in the recent global surface warming slowdown. *Nat. Clim. Change* **6**, 936–940 (2016).
20. Dittus, A. J., Hawkins, E., Robson, J., Smith, D. M. & Wilcox, L. J. Drivers of recent North Pacific decadal variability: the role of aerosol forcing. *Earths Future* **9**, e2021EF002249 (2021).
21. Liguori, G., McGregor, S., Arblaster, J. M., Singh, M. S. & Meehl, G. A. A joint role for forced and internally-driven variability in the decadal modulation of global warming. *Nat. Commun.* **11**, 3827 (2020).
22. Henley, B. J. et al. Spatial and temporal agreement in climate model simulations of the Interdecadal Pacific Oscillation. *Environ. Res. Lett.* **12**, 044011 (2017).
23. Mann, M. E., Steinman, B. A. & Miller, S. K. Absence of internal multidecadal and interdecadal oscillations in climate model simulations. *Nat. Commun.* **11**, 49 (2020).
24. Zhao, Y., Newman, M., Capotondi, A., Lorenzo, E. D. & Sun, D. Removing the effects of tropical dynamics from North Pacific climate variability. *J. Clim.* **34**, 9249–9265 (2021).
25. Heede, U. K. & Fedorov, A. V. Colder Eastern Equatorial Pacific and Stronger Walker Circulation in the early 21st century: separating the forced response to global warming from natural variability. *Geophys. Res. Lett.* **50**, e2022GL101020 (2023).
26. Solomon, A. & Newman, M. Reconciling disparate twentieth-century Indo-Pacific ocean temperature trends in the instrumental record. *Nat. Clim. Change* **2**, 691–699 (2012).
27. Bonfils, C. & Santer, B. D. Investigating the possibility of a human component in various Pacific decadal oscillation indices. *Clim. Dyn.* **37**, 1457–1468 (2011).
28. Scaife, A. A. & Smith, D. A signal-to-noise paradox in climate science. *npj Clim. Atmos. Sci.* **1**, 28 (2018).
29. Eade, R. et al. Do seasonal-to-decadal climate predictions underestimate the predictability of the real world? *Geophys. Res. Lett.* **41**, 5620–5628 (2014).
30. Waite, A. J. et al. Observational and model evidence for an important role for volcanic forcing driving Atlantic multidecadal variability over the last 600 years. *Geophys. Res. Lett.* **47**, e2020GL089428 (2020).
31. Hoesly, R. M. et al. Historical (1750–2014) anthropogenic emissions of reactive gases and aerosols from the Community Emissions Data System (CEDS). *Geosci. Model Dev.* **11**, 369–408 (2018).
32. Frankignoul, C., Sennéchael, N., Kwon, Y.-O. & Alexander, M. A. Influence of the meridional shifts of the Kuroshio and the Oyashio extensions on the atmospheric circulation. *J. Clim.* **24**, 762–777 (2011).
33. Anderson, B. T. Empirical evidence linking the Pacific decadal precession to Kuroshio extension variability. *J. Geophys. Res. Atmos.* **124**, 12845–12863 (2019).
34. Di Lorenzo, E. et al. Modes and mechanisms of Pacific decadal-scale variability. *Annu. Rev. Marine Sci.* **15**, 249–275 (2023).
35. Fenske, T. & Clement, A. No internal connections detected between low frequency climate modes in North Atlantic and North Pacific basins. *Geophys. Res. Lett.* **49**, e2022GL097957 (2022).
36. Broccoli, A. J., Lau, N.-C. & Nath, M. J. The cold ocean-warm land pattern: model simulation and relevance to climate change detection. *J. Clim.* **11**, 2743–2763 (1998).
37. Laguë, M. M., Quetin, G. R. & Boos, W. R. Downwind control of oceanic air by land: the land wake and its sensitivity to CO_2. *Environ. Res. Lett.* **17**, 104045 (2022).

38. Kwon, Y.-O. & Deser, C. North Pacific decadal variability in the Community Climate System Model version 2. *J. Clim.* **20**, 2416–2433 (2007).
39. Smirnov, D., Newman, M., Alexander, M. A., Kwon, Y.-O. & Frankignoul, C. Investigating the local atmospheric response to a realistic shift in the Oyashio sea surface temperature front. *J. Clim.* **28**, 1126–1147 (2015).
40. Seager, R. et al. Strengthening tropical Pacific zonal sea surface temperature gradient consistent with rising greenhouse gases. *Nat. Clim. Change* **9**, 517–522 (2019).
41. Maher, N. et al. The future of the El Niño–Southern Oscillation: using large ensembles to illuminate time-varying responses and inter-model differences. *Earth Syst. Dyn.* **14**, 413–431 (2023).
42. Clement, A. C., Seager, R., Cane, M. A. & Zebiak, S. E. An ocean dynamical thermostat. *J. Clim.* **9**, 2190–2196 (1996).
43. Lehner, F., Deser, C., Simpson, I. R. & Terray, L. Attributing the U.S. Southwest's recent shift into drier conditions. *Geophys. Res. Lett.* **45**, 6251–6261 (2018).
44. Seager, R. & Ting, M. Decadal drought variability over North America: mechanisms and predictability. *Curr. Clim. Change Rep.* **3**, 141–149 (2017).
45. McCabe, G. J. & Dettinger, M. D. Decadal variations in the strength of ENSO teleconnections with precipitation in the western United States. *Int. J. Climatol.* **19**, 1399–1410 (1999).
46. Scaife, A. A. et al. Does increased atmospheric resolution improve seasonal climate predictions? *Atmos. Sci. Lett.* **20**, e922 (2019).
47. Hardiman, S. C. et al. Missing eddy feedback may explain weak signal-to-noise ratios in climate predictions. *npj Clim. Atmos. Sci.* **5**, 57 (2022).
48. Siqueira, L. & Kirtman, B. P. Atlantic near-term climate variability and the role of a resolved Gulf Stream. *Geophys. Res. Lett.* **43**, 3964–3972 (2016).
49. Zhang, W., Kirtman, B., Siqueira, L., Clement, A. & Xia, J. Understanding the signal-to-noise paradox in decadal climate predictability from CMIP5 and an eddying global coupled model. *Clim. Dyn.* **56**, 2895–2913 (2021).
50. Murphy, L. N., Klavans, J. M., Clement, A. C. & Cane, M. A. Investigating the roles of external forcing and ocean circulation on the Atlantic multidecadal SST variability in a large ensemble climate model hierarchy. *J. Clim.* **34**, 4835–4849 (2021).
51. Rayner, N. A. et al. Global analyses of sea surface temperature, sea ice, and night marine air temperature since the late nineteenth century. *J. Geophys. Res. Atmos.* **108**, 4407 (2003).
52. Jeffrey, S. et al. Australia's CMIP5 submission using the CSIRO-Mk3.6 model. *Aust. Meteor. Oceanogr. J.* **63**, 1–13 (2013).
53. Rodgers, K. B., Lin, J. & Frölicher, T. L. Emergence of multiple ocean ecosystem drivers in a large ensemble suite with an Earth system model. *Biogeosciences* **12**, 3301–3320 (2015).
54. Kirchmeier-Young, M. C., Zwiers, F. W. & Gillett, N. P. Attribution of extreme events in Arctic sea ice extent. *J. Clim.* **30**, 553–571 (2017).
55. Sun, L., Alexander, M. & Deser, C. Evolution of the global coupled climate response to Arctic sea ice loss during 1990–2090 and its contribution to climate change. *J. Clim.* **31**, 7823–7843 (2018).
56. Maher, N. et al. The Max Planck Institute Grand Ensemble: enabling the exploration of climate system variability. *J. Adv. Model. Earth Syst.* **11**, 2050–2069 (2019).
57. Rodgers, K. B. et al. Ubiquity of human-induced changes in climate variability. *Earth Syst. Dyn.* **12**, 1393–1411 (2021).
58. Delworth, T. L. et al. SPEAR: the next generation GFDL modeling system for seasonal to multidecadal prediction and projection. *J. Adv. Model. Earth Syst.* **12**, e2019MS001895 (2020).
59. Bonnet, R. et al. Presentation and evaluation of the IPSL-CM6A-LR ensemble of extended historical simulations. *J. Adv. Model.Earth Syst.* **13**, e2021MS002565 (2021).
60. Tatebe, H. et al. Description and basic evaluation of simulated mean state, internal variability, and climate sensitivity in MIROC6. *Geosci. Model Dev.* **12**, 2727–2765 (2019).
61. Fyfe, J. C., Kharin, V. V., Santer, B. D., Cole, J. N. S. & Gillett, N. P. Significant impact of forcing uncertainty in a large ensemble of climate model simulations. *Proc. Natl Acad. Sci. USA* **118**, e2016549118 (2021).
62. Ziehn, T. et al. The Australian Earth system model: ACCESS-ESM1.5. *J. S. Hemi. Earth Syst. Sci.* **70**, 193–214 (2020).
63. Hirahara, S., Ishii, M. & Fukuda, Y. Centennial-scale sea surface temperature analysis and its uncertainty. *J. Clim.* **27**, 57–75 (2014).
64. Gillett, N. P. et al. The Detection and Attribution Model Intercomparison Project (DAMIP v1.0) contribution to CMIP6. *Geosci. Model Dev.* **9**, 3685–3697 (2016).
65. Schneider, U. et al. GPCC's new land surface precipitation climatology based on quality-controlled in situ data and its role in quantifying the global water cycle. *Theor. Appl. Climatol.* **115**, 15–40 (2014).

Methods

Models

We study an extremely large collection of climate model simulations from the past two generations of model development[52–62] (Extended Data Table 1). This collection is composed of simulations from 13 individual climate models. We choose models that have at least 20 publicly available simulations each. All simulations are forced with the best estimates of observed external forcing for the full length of each run. The climate trajectory in each simulation is composed of a unique sequence of internally generated variability not necessarily correlated with the observed variability, plus an externally forced response common to all simulations. The forced response includes both anthropogenic global warming and regional climate changes and is isolated by averaging changes in a given climate variable, such as SST, across many simulations[66]. We consider the time period common to all members, 1950–2014. Note that for CMIP5 models, 2006–2014 is forced with scenario forcing, not observations. We also consider single-forcing runs from DAMIP[64] (Extended Data Table 1). As mentioned in the main text, each of these runs is forced with one time-varying source of external forcing (industrial aerosols, greenhouse gases or natural sources), whereas the others remain constant.

Observations

We compare the simulations used in this study to the PDO index as calculated by the National Oceanic and Atmospheric Administration (NOAA) National Centers for Environmental Information, using the Extended Reconstructed Sea Surface Temperature v.5 of NOAA[67]. To check for robustness, we recalculate the PDO index from the gridded Hadley Centre Sea Ice and Sea Surface Temperature (HadISST) dataset[51]. Both indices are highly similar; we use the HadISST PDO index for display. This SST dataset is also used for the observed temperature maps presented herein. To consider the pattern and strength of the atmospheric circulation over the North Pacific, we use NCEP/NCAR Twentieth Century Reanalysis v.2c (ref. 63). For estimates of southwestern US precipitation, we use a 1° × 1° configuration of the Global Precipitation Climatology Project v.2018 (GPCP) gridded monthly precipitation product covering the years 1901–2014 (ref. 65).

Indices

In each individual simulation, we first calculate monthly SST anomalies relative to the climatological seasonal cycle. We next calculate the PDO index as the first EOF of North Pacific (20°–80° N) monthly SST anomalies, after subtracting the global mean SST anomaly from each month at each grid point[2]. We choose this index because of its historical and ongoing value in forecasting climate impacts[1,2,68]. Furthermore, by removing global mean SST, we show that the relationship between forcing and the PDO is more than the obvious GHG-induced warming trend. An alternative definition of the PDO index that removes North Pacific average SSTs instead of global average SST yields qualitatively similar results for the metrics we put forward in the main text and Extended Data Fig. 2. To calculate the forced component of the PDO index in models, we average each of these individual PDO indices together. We follow the convention that the PDO is positive when there is warming along the coast of North America paired with cooling off the coast of Japan[3]. The Kuroshio–Oyashio Extension Index is calculated as the linearly detrended, area-weighted average SST between 25°–35° N and 150°–180° E (ref. 5). The North Pacific Index, a measure of Aleutian Low strength is calculated as the area-weighted average sea-level pressure between 35°–65° N and 160° E–140° W (ref. 69). The precipitation index of the western United States is the water-year average (October to September), area-weighted average total precipitation between 31°–42° N and 125°–110° W, over land (following ref. 43). ENSO is summarized using the Niño 3.4 Index, the area-weighted average monthly SST anomalies in the tropical Pacific (5° S–5° N, 170° W–120° W). The forced component of each of these indices is calculated as the average across all simulations of the individual indices. The externally forced temperature, pressure and precipitation maps are calculated by first finding the ensemble mean field and then calculating any appropriate regression. In this construction of the ensemble mean, each ensemble member, not each model, is weighted equally. All time series are low-pass filtered using a 100-point Lanczos filter with a 1/10 year half-power frequency, unless otherwise noted. Endpoints are padded with the mean of the timeseries. Other approaches, including padding with zeros, repeating endpoints and removing endpoints, were all tested and did not affect our results. For the observed PDO index, we remove the ENSO signal using linear regression. This simple method probably does not fully remove the influence of ENSO on the PDO[24].

Statistical significance

Throughout this study, we test several complementary null hypotheses to ensure robustness and transparency in our results. These tests seek to account for the limited number of degrees of freedom afforded by short time series with high autocorrelations:

1. Testing the null hypothesis that the Pearson correlation coefficient is equal to zero: each of the time series presented in this work has strong autocorrelation. To account for this, we use a commonly used empirical statistical test[70]. This test creates surrogate ensemble mean PDO time series by re-shuffling the phases of its periodogram. Each surrogate time series, therefore, has the same autocorrelation structure as the original time series. We correlate the surrogate time series with the observed time series and repeat the process 10,000 times to create a distribution. We calculate a *P*-value by comparing the original correlation to this distribution.
2. Testing the null hypothesis that the correlation between the ensemble mean and observations is a chance result of internal variability: this test is a corollary to the null hypothesis that the correlation coefficient is zero but tests the correlation against realizations of internal variability generated by the models rather than statistically generated realizations. This approach allows our test to account for the differences in the temporal structure of internal variability, as estimated by the model. To isolate internal variability, we remove the ensemble mean PDO from the PDO index in each individual member (as in Fig. 2a). We then correlate the observed time series with each model-generated realization of internal variability to create a distribution. We calculate the significance level by comparing the original correlation to this distribution.
3. Testing the null hypothesis that the forced correlation is a result of the chance alignment between the forced response of the model and internal variability: here we correlate the PDO index with the PDO index from each individual ensemble member to create a distribution. We calculate the significance level by comparing the original correlation to this distribution.
4. Testing the null hypothesis that the ensemble mean is effectively isolating the forced response: here, we randomly resample individual model runs (with replacement) 10,000 times to construct new 100-member ensembles. We then create 10,000 new ensemble mean PDO indices and correlate each of them with observations to create a distribution. We use this distribution to construct confidence intervals. Using this approach, we find that the average ensemble mean PDO index from a 572-member ensemble produces a correlation of 0.71 (95% confidence interval: 0.66–0.76) with observations. Likewise, we find that the average ensemble mean KOE SST index from a 572-member ensemble produces a correlation of 0.57 (95% confidence interval: 0.51–0.62) with observations. The mean values are slightly different from the full ensemble values presented in the text because we resample with replacement. In Fig. 2d, we extend this approach to test different ensemble sizes.

In this study, each assertation is typically subject to several of these tests, as appropriate.

Estimating the signal-to-total variance ratios in models and observations

We are interested in isolating the role of forcing in observations but are only privy to one realization of the climate of Earth. The (unknowable) true forced response $O_F(t)$, is a component of the observed timeseries:

$$O(t) = O_F(t) + O_I(t)$$

where $O_I(t)$ is the (unknowable) internally generated variability in the observed time series. We estimate the forced response by a regression on the ensemble mean EM(t) of model runs

$$O_F(t) = \beta \mathrm{EM}(t) + \epsilon$$

The fraction of observed variance explained by this regression model is

$$R_i^2 \equiv \frac{\sigma_F^2}{\sigma_O^2} \approx \frac{\sigma_{EM}^2}{\sigma_O^2}$$

where σ_F^2 is the (unknowable) forced variance, σ_O^2 is the total observed variance and σ_{EM}^2 is the variance of the model ensemble mean.

Unlike observations, in large ensembles, we know the ratio of forced-to-total variability, R_j^2. We estimate it as the variance of the ensemble mean, σ_{EM}^2, divided by the average of the total variance in each ensemble member, σ_E^2:

$$R_j^2 = \frac{\sigma_{EM}^2}{\sigma_E^2}$$

There are other ways to estimate this fraction of model variance that is forced; for example, we could find R_j as the average correlation of each of the ensemble members with the ensemble mean. As ensemble size j increases, the various estimates converge asymptotically, and with our sample size of 572, the differences are negligible ($R < 0.01$). As we discuss in the text and show in Extended Data Table 3, our estimate of the observed forced variance ratio, R_i^2, is much larger than the ratio that we estimate from our large ensemble, R_j^2. It follows that the (estimated) observed signal-to-noise ratio, $R_i^2/(1-R_i^2)$ is even larger compared with the model signal-to-noise ratio, $R_j^2/(1-R_j^2)$. The mismatch between these two ratios is known as the signal-to-noise paradox[28,29].

Novel attribution technique that accounts for the signal-to-noise error in climate models

To estimate the impacts of the forced PDO, we statistically correct for this signal-to-noise error in models. We do so by rescaling the variance of the multidecadal, forced PDO and its impacts in each simulation so that the signal-to-total ratio of the PDO index is the same as that in the observations. As in most applications of imperfect models to nature, we have already corrected for the mean state by using anomalies and correcting for overall amplitude error by rescaling using observed variance. We use this rescaled model output to better understand forced PDO impacts, for instance, precipitation in the western United States. We label this impact variable X; it is the sum of a component X_{fPDO} that is a response to the forced PDO and an unforced component X_{res}. We find X_{fPDO} by linearly regressing X on the PDO index. X_{res} is then the residual $X - X_{fPDO}$. We separate this resultant field, X_{res}, into low-frequency X_{LP} and high-frequency components X_{HP}, by low-pass filtering the time series at each grid point. We then rescale both the forced component related to the PDO and the remaining low-frequency component so that the signal-to-noise ratio in the model matches that estimated for the observations; that is,

$$X' = \sqrt{\frac{R_j^2}{R_i^2}} \times X_{fPDO} + \sqrt{\frac{1-R_j^2}{1-R_i^2}} \times X_{LP} + X_{HP}$$

Note that the higher-frequency variance (residual after low-pass filtering) remains at its original amplitude and that the total LP variance is unchanged. The assumption that total variance remains constant affects the width of the resultant distributions, but not our ensemble mean results. We retain the model-generated high-frequency variance to ensure the strongest possible tests of our results.

There are multiple potential sources of uncertainty in our estimate of the signal-to-noise ratio used for this recalibration. A testable source of uncertainty is the possibility that internal variability in observations aligns with the ensemble mean to artificially inflate our estimate of the observed signal-to-noise ratio. For our estimate of the signal-to-noise ratio in observations ($R^2/(1-R^2)$, $0.53/(1-0.53) = 1.13$) to be so wrong as to be the same as in models ($0.07/(1-0.07) = 0.08$), the correlation between the ensemble mean and internal variability must exceed 0.62. This occurs in 1 out of our 572 ensemble members. This potentially thorny ensemble member simulates a 3.48% per 30 years increase in precipitation between 1983 and 2012 (relative to a 13.3% decrease in precipitation in observations). So, even if we accept the small chance that internal variability has confounded our understanding of the forced PDO—in this one extreme example present in the large ensemble—it does not explain the observed drought nor detract from our argument that the drought will continue to be forced moving forward.

Data availability

All climate model output is publicly available at the Earth System Grid Federation (https://esgf.llnl.gov/). NOAA Extended Reconstructed SST v.5 (ERSSTv5), NOAA/CIRES/DOE 20th Century Reanalysis (v.3) and Global Precipitation Climatology Project (GPCP) Monthly Analysis Product data provided by the NOAA PSL at https://psl.noaa.gov. Hadley Centre Sea Ice and Sea Surface Temperature (HadISST) data were provided by the Met Office (United Kingdom) and are available at https://www.metoffice.gov.uk/hadobs/hadisst/. This study used the MATLAB Mapping Toolbox to construct maps, including the Coastlines dataset[71].

Code availability

This study used MATLAB and the MATLAB Signal Processing Toolbox and the Statistics and Machine Learning Toolbox for statistical analysis. This included the use of code from the WEACLIM toolbox, available on the MATLAB File Exchange[72]. The code used to perform the statistical tests and produce the figures is available at Zenodo[73] (https://doi.org/10.5281/zenodo.15658555).

66. Kay, J. E. et al. The Community Earth System Model (CESM) large ensemble project: a community resource for studying climate change in the presence of internal climate variability. *Bull. Am. Meteorol. Soc.* **96**, 1333–1349 (2015).
67. Huang, B. et al. Extended Reconstructed Sea Surface Temperature, Version 5 (ERSSTv5): upgrades, validations, and intercomparisons. *J. Clim.* **30**, 8179–8205 (2017).
68. Mantua, N. J. & Hare, S. R. The Pacific decadal oscillation. *J. Oceanogr.* **58**, 35–44 (2002).
69. Trenberth, K. E. & Hurrell, J. W. Decadal atmosphere-ocean variations in the Pacific. *Clim. Dyn.* **9**, 303–319 (1994).
70. Ebisuzaki, W. A method to estimate the statistical significance of a correlation when the data are serially correlated. *J. Clim.* **10**, 2147–2153 (1997).
71. MATLAB. *Signal Processing Toolbox* (MathWorks, 2023).
72. Moron V. *WEACLIM*. https://www.mathworks.com/matlabcentral/fileexchange/10881-weaclim. (MATLAB Central File Exchange, 2025).
73. Klavans, J. M. jeklavans/PDO_2024: human emissions drive recent trends in North Pacific climate variations (v1.0). *Zenodo* https://doi.org/10.5281/zenodo.15658555 (2025).

Acknowledgements We thank J. Fasullo, J. Kay and I. Simpson for their comments. We acknowledge the grants received from the National Science Foundation (grant AGS-2002528)

(J.M.K., P.N.D. and T.M.S.), the NOAA Climate Program Office (grant NA20OAR4310400) and the National Science Foundation (grant AGS-2241752) (A.C.C.). The National Center for Atmospheric Research is sponsored by the National Science Foundation.

Author contributions J.M.K. and P.N.D. conceptualized the study. J.M.K., P.N.D. and M.A.C. devised the methodology. J.M.K. conducted the investigation. J.M.K. performed the visualization. P.N.D. and T.M.S. helped with the funding acquisition. J.M.K. wrote the original draft. J.M.K., P.N.D., A.C.C., C.D., T.M.S. and M.A.C. wrote, reviewed and edited the paper.

Competing interests The authors declare no competing interests.

Additional information

Supplementary information The online version contains supplementary material available at https://doi.org/10.1038/s41586-025-09368-2.

Correspondence and requests for materials should be addressed to Jeremy M. Klavans.

Peer review information *Nature* thanks Guillaume Gastineau and the other, anonymous, reviewer(s) for their contribution to the peer review of this work. Peer reviewer reports are available.

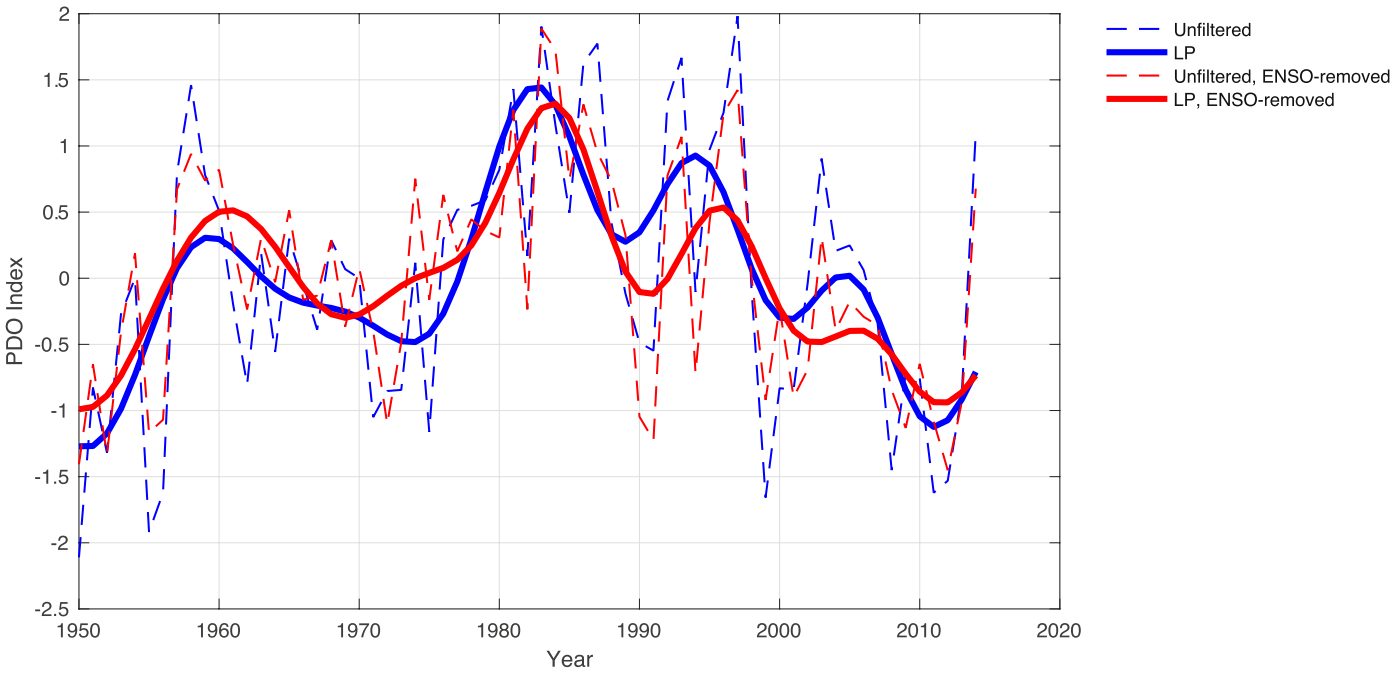

Extended Data Fig. 1 | The limited effect of ENSO removal on the observed PDO index. Observed PDO index timeseries (from NOAA) with and without linearly-removing ENSO for unfiltered (annual average) and low-pass (LP) filtered data.

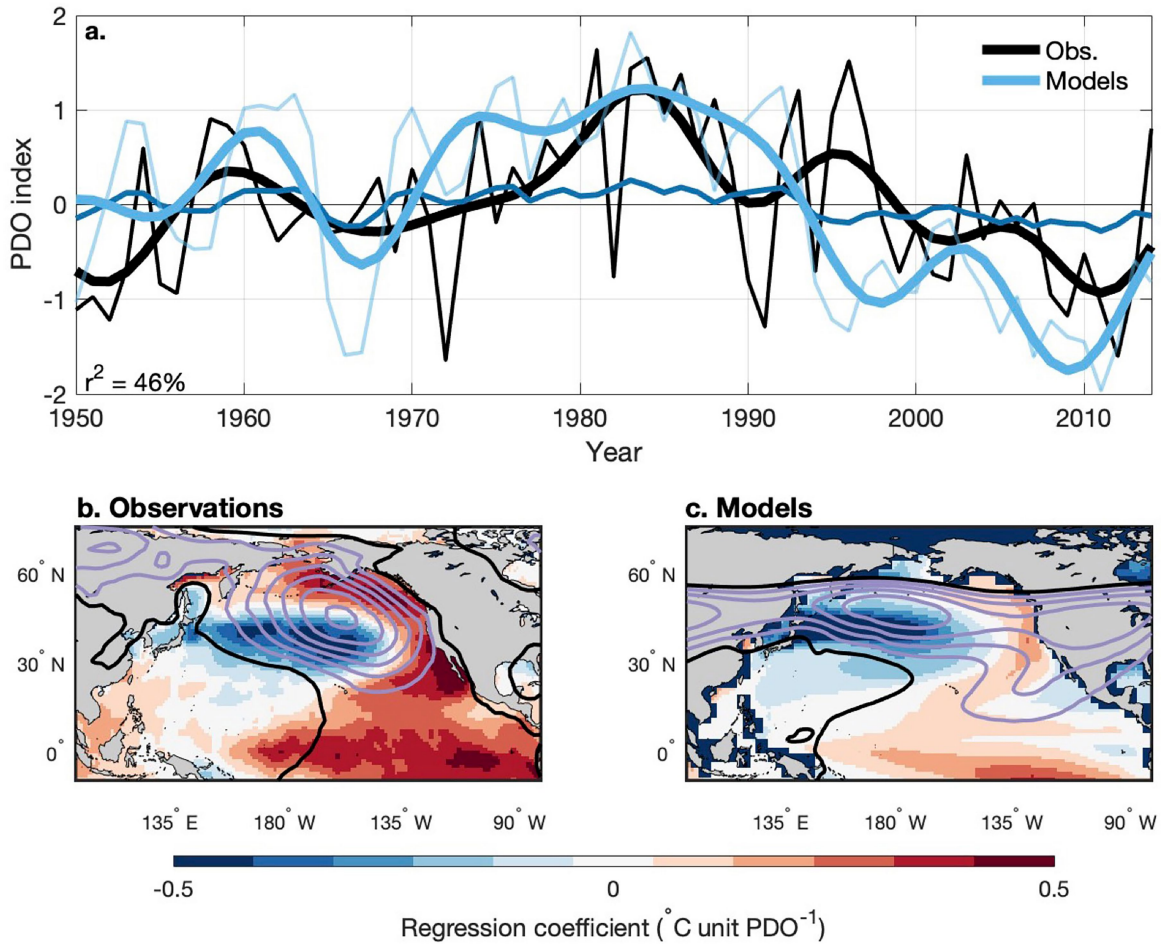

d

	Unfiltered Corr. (Sig. Level)	Low-pass Filtered Corr. (Sig. Level)
PDO (GMSST Removed)	0.43 (6%)	0.73 (4%)
PDO (North Pacific Removed)	0.36 (8%)	0.69 (6%)
KOE SST Index	0.34 (9%)	0.68 (4%)

Extended Data Fig. 2 | The forced component of the PDO is relatively insensitive to the PDO index definition. The PDO index in all panels is defined as the 1st principal component of North Pacific sea-surface temperatures after removing North Pacific average SSTs (Methods). **a**, The observed PDO index (black) compared with the ensemble mean PDO index from the all-forcings simulations (dark blue) and the normalized ensemble mean PDO index from the all-forcings simulations (light blue). We normalize the forced PDO index strictly to illustrate the timing of the shifts in both indices; the amplitudes of each timeseries are listed in Extended Data Table 2 and discussed in-text. **b**, Regression of observed SST (colours) and sea-level pressure (contours; hPa per unit of the PDO index) on the observed PDO index. We draw contours every −0.5 hPa in purple; the zero contour is in black. The KOE region is outlined in solid black. **c**, Regression of forced SST (colours) and sea-level pressure (contours) on the normalized, forced PDO index. **d**, Correlation coefficients and their significance levels for the three PDO definitions in the main text. As in the main text, the KOE SST index is detrended. Significance levels are calculated empirically via phase re-shuffling (Methods).

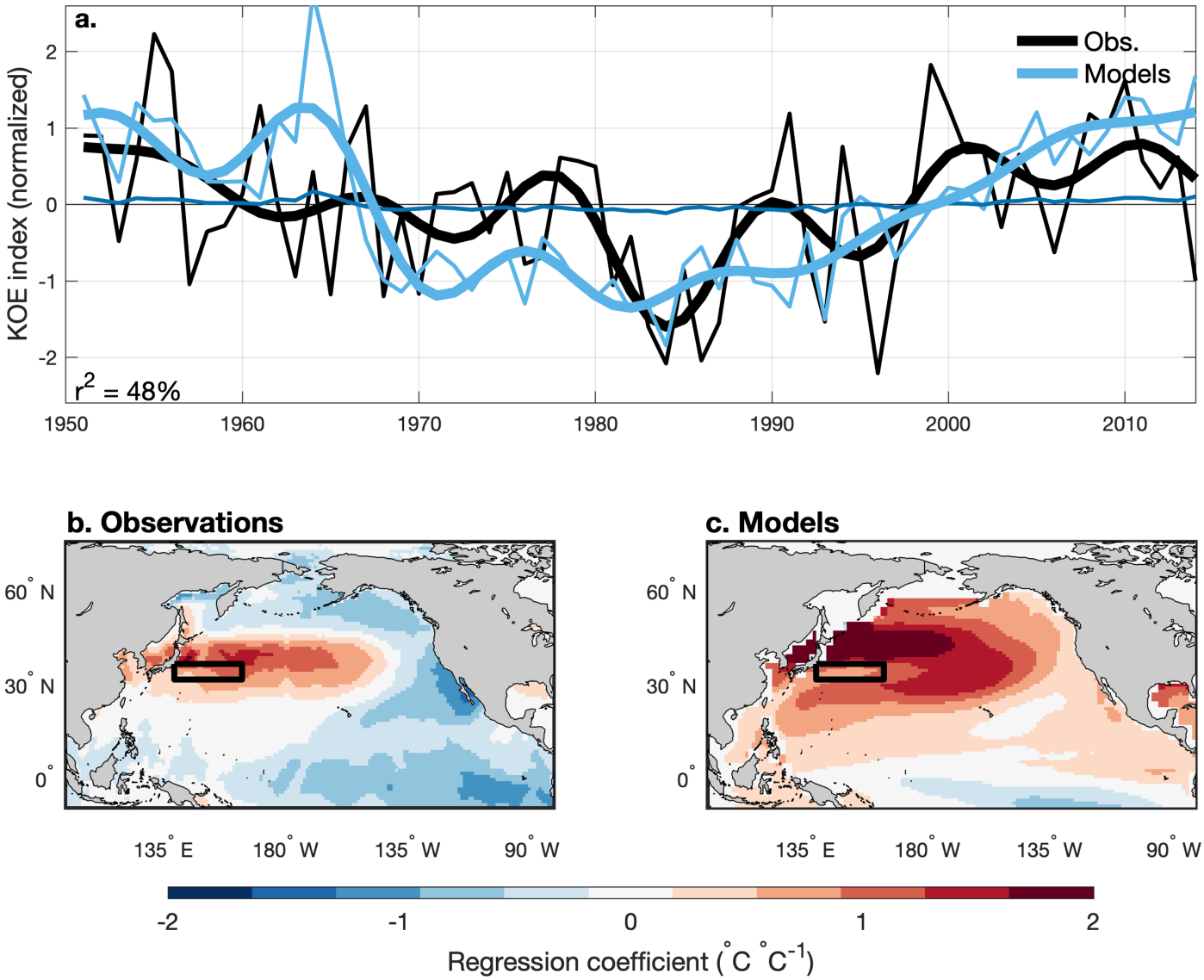

Extended Data Fig. 3 | The role of external forcing is similar in a N. Pacific sea-surface temperature index. An index of linearly detrended, spatial-average sea-surface temperatures in the Kuroshio-Oyashio Extension region of the North Pacific is calculated (31° – 36° N, 140° – 165° E; black outline) and regressed on SSTs in observations and models, which shows that the forced signal described in-text is not an artifact of the method we use to calculate the PDO index. **a**, The detrended, observed KOE sea-surface temperature index (black) compared and the detrended ensemble mean KOE SST index (dark blue) and the normalized, detrended, ensemble mean KOE SST index from the all-forcings simulations (light blue). We normalize the forced KOE index strictly to illustrate the timing of the shifts in both indices; the amplitudes of each timeseries are listed in Extended Data Table 2 and discussed in-text. **b**, Regression of observed SST (colours) on the observed, detrended, KOE index. **c**, Regression of forced SST (colours) on the normalized, detrended, forced KOE index.

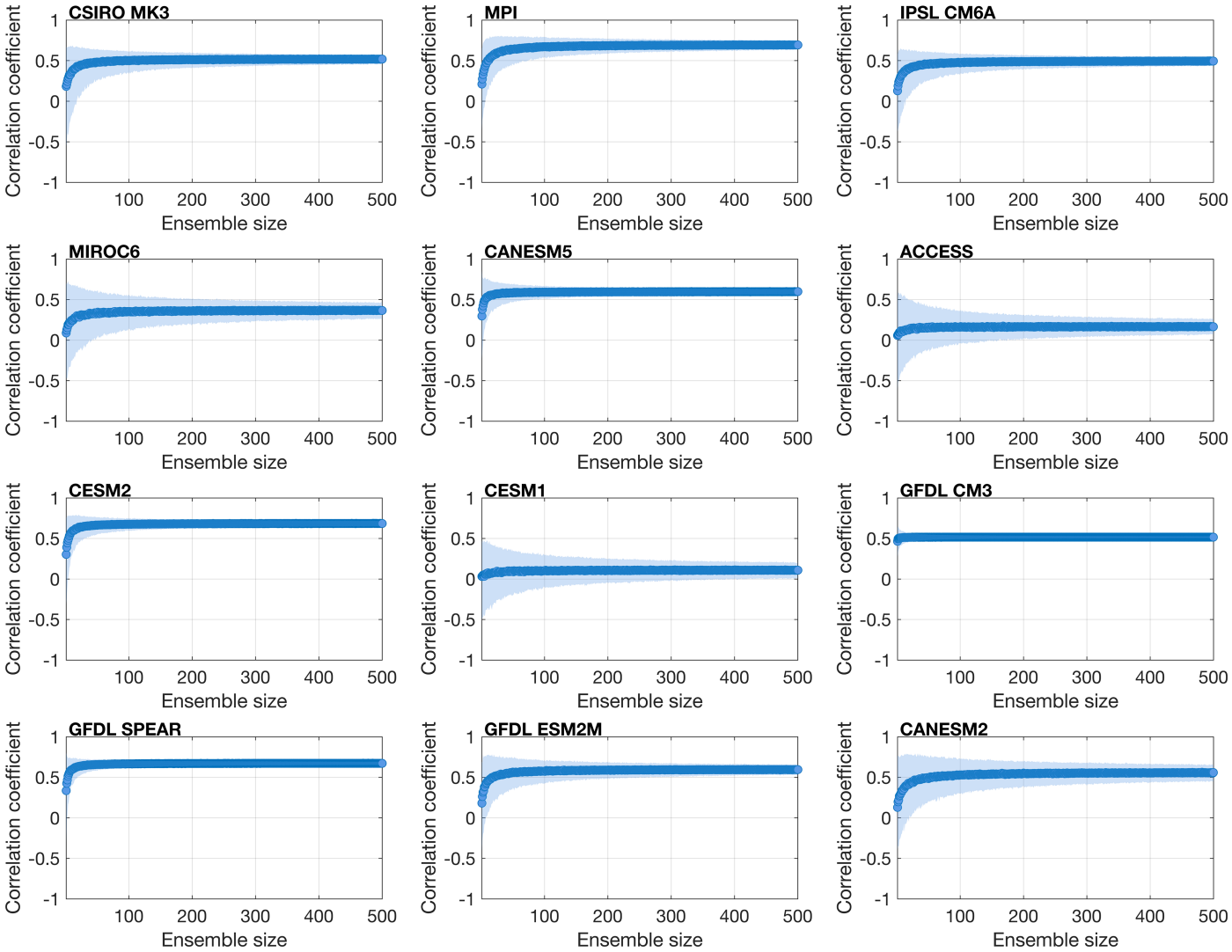

Extended Data Fig. 4 | There is a meaningful forced component in the PDO in most single-model large ensembles. All panels: for each ensemble size, in each single model large ensemble, we randomly select members from the full ensemble (with replacement), average, and correlate with observations to calculate the mean correlation coefficient (dot) and the 95% confidence interval (cloud). Please note that this figure reports the correlation coefficient not its square, explained variance (as in Fig. 2d), because some values are negative. Additionally, re-sampling with replacement may give a false sense of stability and significance for the correlations calculated from smaller ensembles.

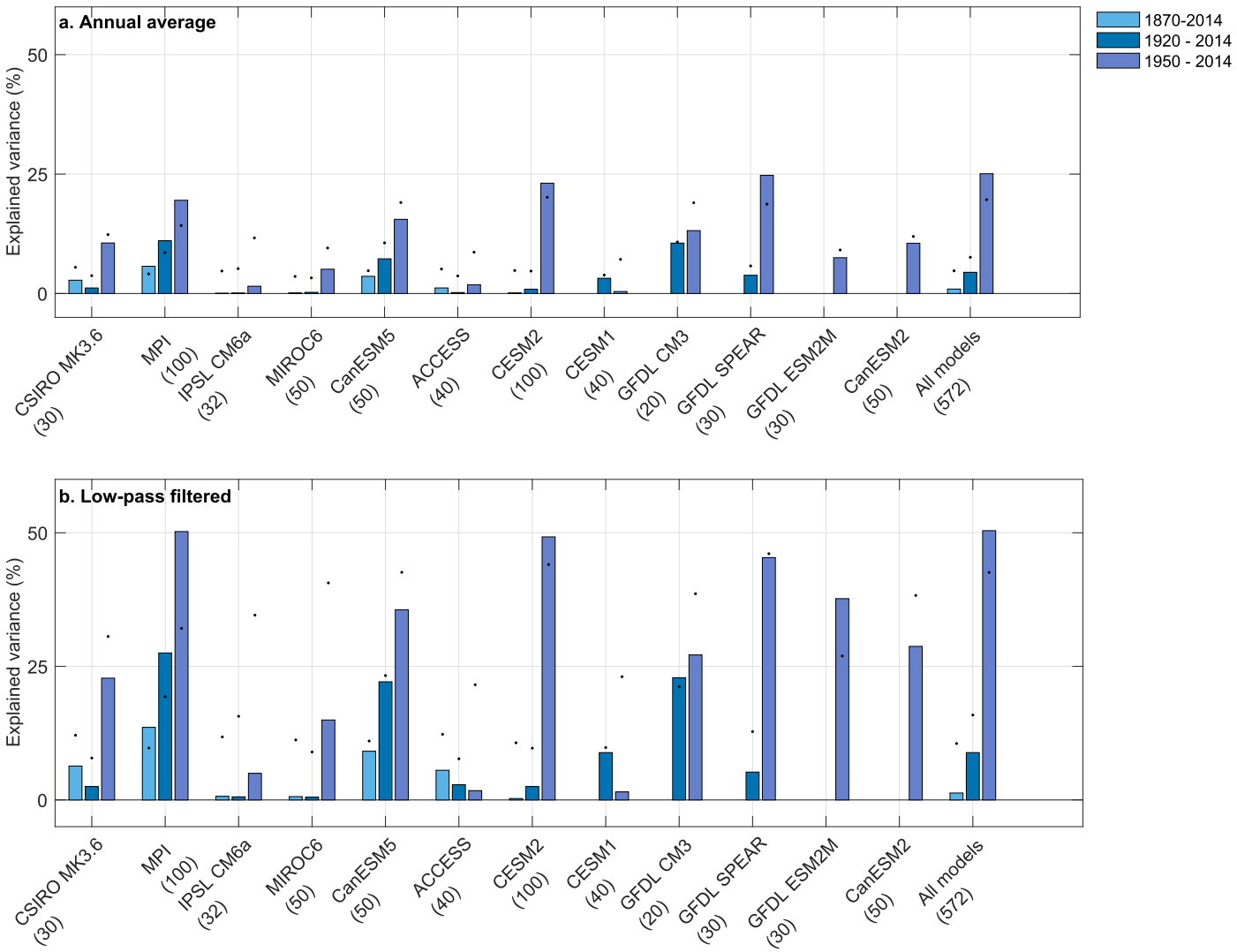

Extended Data Fig. 5 | As forcing intensifies, the role of forcing in the PDO grows larger. a,**b**, External forcing explains more PDO variance after 1950 on both (**a**) interannual and (**b**) multidecadal timescales. Please note we only plot bars where model output allows; not all models were initialized in or before 1870 (see Extended Data Table 1). Also, the number of simulations in each single-model ensemble varies (listed below model name and in Extended Data Table 1) implying that these bars may not be directly comparable to each other, especially for those models with fewer simulations. Please note that the "all models" value varies slightly from the text because we calculate the first principal component of North Pacific SST earlier than 1950 in those models that allow. The black dots correspond to the empirical 90% confidence level, as calculated via phase re-shuffling (Methods).

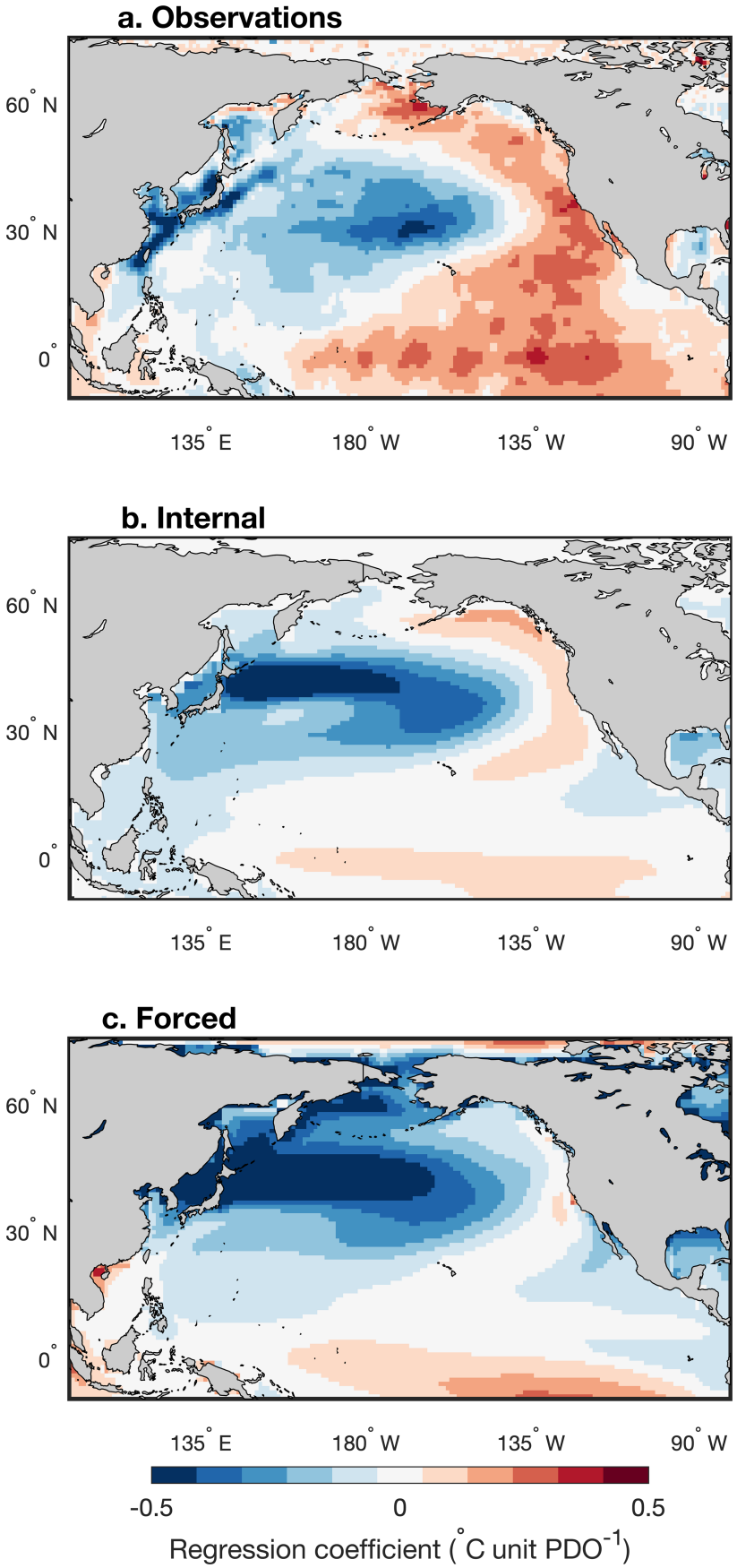

Extended Data Fig. 6 | See next page for caption.

Extended Data Fig. 6 | The model-generated internal and forced PDO patterns appear similar to observations and each other. a, Regression of observed SST on the observed PDO index. **b**, The average regression pattern of the internal PDO SST pattern across all ensemble members. In each ensemble member, we calculate the regression of SST on the PDO index at each grid point. We then average these regression patterns across the full multi-model ensemble with each member weighted equally. **c**, Regression of ensemble mean SST on the normalized, ensemble mean PDO index from the all-forcings simulations.

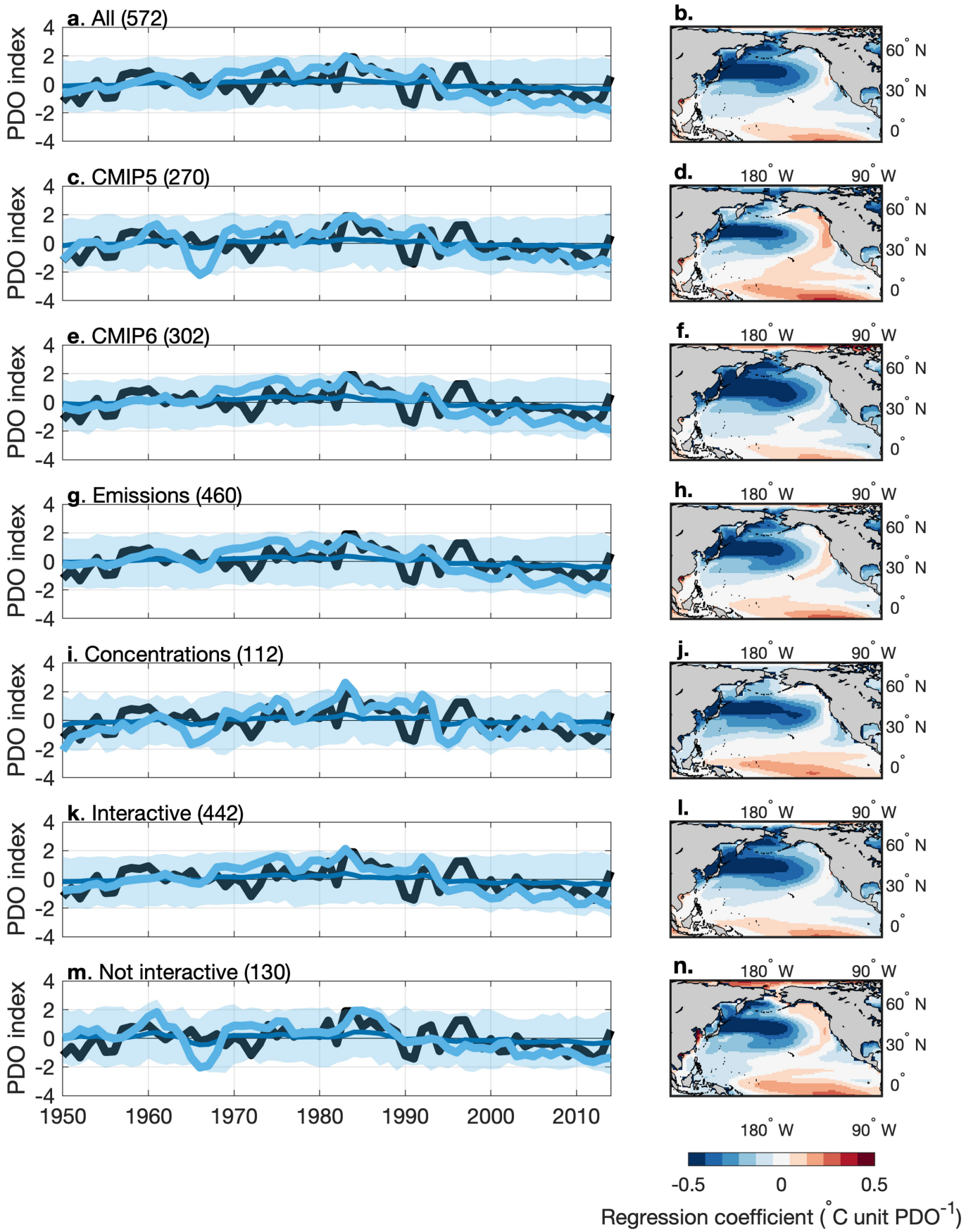

Extended Data Fig. 7 | See next page for caption.

Extended Data Fig. 7 | The explanatory power of the forced PDO is not sensitive to model configuration. Left panels: the observed PDO index (black) compared with the ensemble mean PDO index from the all-forcings simulations (dark blue), the normalized ensemble mean PDO index from the all-forcings simulations (light blue), and the two standard deviation ensemble spread from the all-forcings simulations (blue cloud). Right panels: regression of ensemble mean SST (colours) on the normalized, ensemble mean PDO index. The number of members in each ensemble is listed in parentheses next to the description.

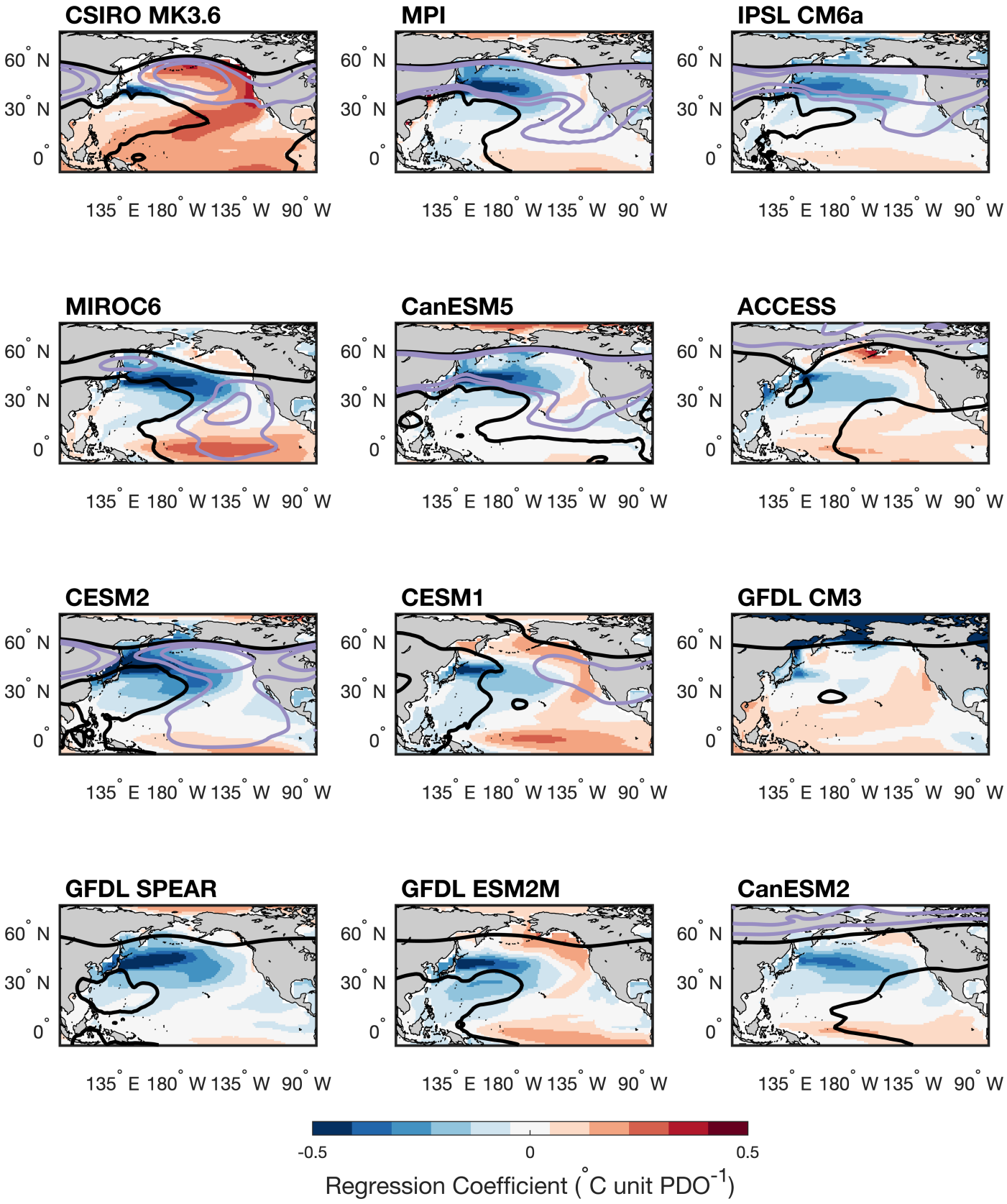

Extended Data Fig. 8 | The forced PDO pattern in each large single-model large ensemble. All panels: regression of ensemble mean SST on the normalized, ensemble mean PDO index from each single model large ensemble we consider.

Extended Data Table 1 | Components of the multi-model large ensemble

All-forcings					
CMIP5 Ensembles	Atmospheric resolution	# of members (270)	Start year	Emissions vs. concentrations	Fully-interactive
NCAR-CESM1	1deg	40	1920	Emissions	Yes
GFDL-CM3	2deg	20	1920	Emissions	Yes
GFDL-ESM2M	2deg	30	1950	Concentration	No
CCCma-canESM2	2.8deg	50	1950	Concentration	Yes
CSIRO-Mk3	1.9deg	30	1850	Emissions	Yes
MPI-ESM-LR	1.9deg	100	1850	Emissions	No
CMIP6 Ensembles	Atmospheric resolution	# of members (302)	Start year	Emissions vs. concentrations	Fully-interactive
NCAR-CESM2	1deg	100	1850	Emissions	Yes
GFDL-SPEAR	0.5deg	30	1921	Emissions	Yes
IPSL-CM6A-LR	~2deg	32	1850	Concentration	Yes
MIROC6	~2deg	50	1850	Emissions	Yes
canESM5	~2deg	50	1850	Emissions	Yes
ACCESS-ESM1.5	~1.5deg	40	1850	Emissions	Yes

Single-forcing			
Model	Aerosol-only (75)	GHG-only (82)	Natural-only (129)
canESM5	30	50	50
CNRM-CM6	10	9	10
GISS-E2_1_G	15	10	20
IPSL CM6A LR	10	10	8

Additional details on the climate models studied[52–62,64,66]. Classifications for cloud-aerosol interactions are constructed following[5,14].

Extended Data Table 2 | Decomposition of North Pacific SST variance

a

Forced Variance	1870-1949	1950-2014
PDO Index (Unfiltered)	0.02	0.04
PDO Index (LP)	0.02	0.04
KOE SST Index (Unfiltered)	0.01	0.14
KOE SST Index (LP)	0.01	0.13

b

	Forced Variance	Internal Variance	Total variance (Forced plus Internal)
KOE SST Index (Unfiltered)			
1870 - 1949	0.01	0.36	0.37
1950 - 2014	0.14	0.36	0.50
1870 - 2014	0.08	0.38	0.46
KOE SST Index (LP)			
1870 - 1949	0.01	0.18	0.19
1950 - 2014	0.13	0.18	0.31
1870 - 2014	0.07	0.21	0.28

a, Ensemble mean variance for the PDO index and detrended KOE SST index from the suite of models that were initialized in 1850 (see Extended Data Table 1). Values are reported for both the annual average indices and the low-pass filtered (LP) indices. **b**, Forced, internal, and total variance in the unfiltered and low-pass filtered (LP) KOE SST index, spliced by time period. The internal variance is calculated by subtracting the ensemble mean KOE SST index from each individual ensemble member's detrended KOE SST index, as in the main text.

Extended Data Table 3 | The signal-to-noise error in response to external forcing

All-Forcings							
Name	# members	R^2 (1950 – 1989)	R^2 (1990 – 2014)	R^2 (1950 – 2014)	S:T PDO	S:T KOE SST	S:T NPI
All	572	0.43 (0.01)	0.35 (0.14)	0.53 (0.02)	0.19	0.27	0.09
CMIP5	270	0.51 (0.01)	0.35 (0.14)	0.59 (0.01)	0.15	0.20	0.09
CMIP6	302	0.28 (0.03)	0.36 (0.14)	0.44 (0.05)	0.25	0.34	0.11
Emissions	460	0.37 (0.02)	0.44 (0.12)	0.50 (0.02)	0.21	0.28	0.11
Concentrations	112	0.57 (0.01)	0.03 (0.35)	0.33 (0.07)	0.17	0.23	0.13
Interactive	442	0.35 (0.02)	0.31 (0.15)	0.46 (0.04)	0.20	0.29	0.09
Not interactive	130	0.31 (0.04)	0.58 (0.08)	0.50 (0.01)	0.22	0.27	0.12
Single-Forcing							
Name	Total number of members	R^2 (1950 – 1989)	R^2 (1990 – 2014)	R^2 (1950 – 2014)	S:T PDO (1950-1989)	S:T PDO (1990 -2014)	S:T PDO (1950 - 2014)
Aerosol-only	75	0.58 (<0.01)	0.16 (0.22)	0.04 (0.40)	0.02	0.01	0.02
GHG-only	82	0.60 (<0.01)	0.57 (0.10)	0.09 (0.31)	0.17	0.19	0.45
Natural only	129	0.38 (0.03)	0.00 (0.52)	0.01 (0.38)	0.02	0.01	0.02

The timing and amplitude of the forced PDO for all-forcings ensembles of varying model designs and for the single-forcing ensembles (see Extended Data Table 1). The R^2 columns report the square of the correlation between the ensemble mean and observed PDO indices for the time period indicated along with its significance level. The significance level is calculated empirically as in Fig. 1a, via phase reshuffling of the ensemble mean in frequency space[70]. For the R^2 columns, significance testing was applied to the correlation. Please note that the correlation coefficient between the GHG-only ensemble mean and observations is negative. The signal-to-total ratios estimated in the three right-most columns are calculated as the ratio of forced-to-total variance. The "signal-to-noise paradox", described in Methods, emerges when there is a mismatch between the R^2 values and the signal-to-total ratios. Signal-to-total ratios are reported for the PDO index, KOE SST index, and the North Pacific Index (NPI) for the all-forcings ensembles and for the listed time periods for the single-forcing ensembles.